Contents lists available at ScienceDirect

Electrochimica Acta

journal homepage: www.journals.elsevier.com/electrochimica-acta

Simulating cyclic voltammetry at rough electrodes by the digital-simulation–deconvolution–convolution algorithm

Tim Tichter [a,*], Alex Tichter [b], Dirk Andrae [c], Christina Roth [d]

[a] *Federal Institute of Materials Research and Testing (BAM), Unter den Eichen 87, 12195 Berlin, Germany*
[b] *NKaiX Holding B.V., Groenestraat 294 B002, 6531 JC Nijmegen, Netherlands*
[c] *Physical and Theoretical Chemistry, Freie Universität Berlin, Arnimallee 22, 14195 Berlin, Germany*
[d] *Electrochemical Process Engineering, Universität Bayreuth, Universitätsstr. 30, 95447 Bayreuth, Germany*

ARTICLE INFO

ABSTRACT

The influence of electrode roughness on diffusional cyclic voltammetry (CV) is investigated from a theoretical perspective. For this purpose, the digital-simulation–deconvolution–convolution (DSDC) algorithm, initially developed for the simulation of CV at porous electrodes, is subjected to three substantial modifications. First, by employing adaptive numerical resolution and sample volumina, the computational demand of the digital simulation (DS) step is reduced significantly. Second, by modifying the Douglas–Gunn algorithm of the DS-step to operate on an arbitrarily incremented spatial grid perpendicular to the macroscopically planar electrode surface, the bulk of the fluid can be treated with an exponentially increasing spatial discretization which uses computational power even more efficiently. The third modification is an optimization of the computationally demanding deconvolution step which is used to extract the mass-transfer function from the data computed in the DS-step. This, initially recursive procedure, is replaced by a three-step sequence consisting of (I) a numerical Laplace transformation (NLT) on an exponentially expanding time-grid, (II) a Laplace-domain integration (LDI) and finally (III) a numerical inversion of Laplace transformation (NILT) using the Gaver–Stehfest (GS) inversion formula. Based on this novel strategy for CV simulation, the effects of electrode roughness are thoroughly investigated. It is demonstrated that for an ideally reversible reaction the effects of electrode roughness on the CV response are insignificant at common experimental timescales. In contrast, for scenarios with electrochemically quasi-reversible (or irreversible) kinetics, the apparent rate constants are allegedly upscaled by the area ratio $\psi = A_{\mathrm{rough}}/A_{\mathrm{planar}}$. This manifests in a lower peak-to-peak separation without a distortion of the shape of the voltammetric profile. This behavior is finally explained in a quantitative manner in terms of convolution-sums and mass-transfer functions which ultimately puts the parameter *electrode roughness* into the semianalytical framework of convolutive modeling.

1. Introduction

The current response of diffusional cyclic voltammetry at mesoscopically rough electrode surfaces can differ significantly from the ideally planar scenario. Experimentally, we encountered this phenomenon during electroanalytical studies of the kinetics of the V^{2+}/V^{3+}-redox reaction on metallic bismuth electrodes. While bismuth received an increasing interest in the vanadium redox-flow battery community in recent years [1–7], most studies utilize it in the form of nanoparticles decorated in a porous electrode. In this particular study, however, we utilized a planar working electrode made of elemental bismuth for benchmarking purposes. Starting with an initially rather poor electrochemical activity it was found that the electrode seemingly provided an enhanced electrocatalytic performance after a few tenth of CV cycles. This is illustrated in Fig. 1-(A). There, it can be seen that the voltammetric profile of the cycled bismuth electrode (red curve) possesses a more narrow peak-to-peak separation in comparison to its pristine analogue (black curve) which, following the theory of CV on flat surfaces [8], would be an indicator of an improved kinetics.

While initially speculating on some kind of activation mechanism, scanning electron microscopy revealed that the initially smooth electrode underwent a significant surface restructuring leading to a mesoscopic scale of roughness. This is illustrated in panels (B) to (E) in Fig. 1, and was the main motivation for investigating the interplay of electrode roughness and electrode kinetics from a purely theoretical perspective.

On a first glance, it follows quite naturally that an increase in surface roughness will introduce a larger electrode area exposed to
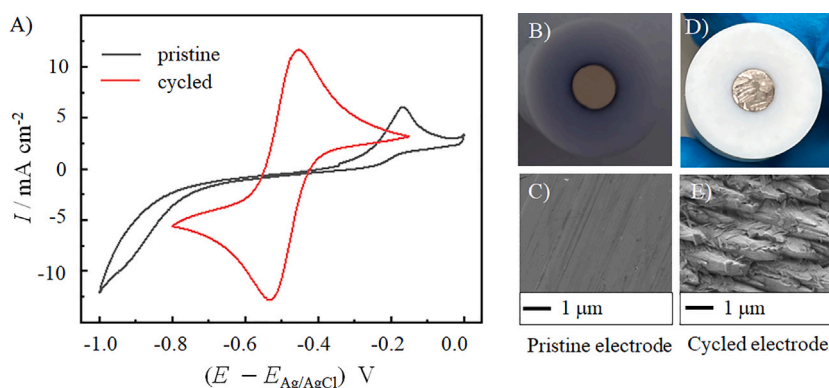

Fig. 1. (A) Cyclic voltammograms recorded for the V^{2+}/V^{3+}-redox reaction at a potential sweep-rate of 20 mV/s at ambient temperature. Potentials were referred to a Ag/AgCl reference electrode. The working electrode was a metallic bismuth disk with a diameter of 5 mm with a smooth (black curve) and rough (red curve) surface. The electrolyte was a degassed aqueous solution containing 0.16 M of the electrochemically active species and 2 M H_2SO_4. Panels (B) and (D) are photographs of the electrode surfaces with (C) and (E) being the corresponding scanning electron microscopy images. It can be seen that the voltammetric profile of the rough electrode shows a much more narrow peak-to-peak separation usually associated with improved electrode kinetics.

the electrolyte. Therefore, when compared to the purely geometrical (projected) surface, it holds $A_{geo} \leq A_{rough}$. Assuming that the intrinsic activity of the electrode material is preserved, one could speculate that this additional surface area will *allegedly* upscale the kinetics by increasing the density of active sites — or more precisely — the active area per unit area. Under mostly semi-infinite diffusion conditions, this should maintain the overall shape of the voltammetric curve while reducing the peak-to-peak separation — exactly as seen in Fig. 1-(A). However, one may also consider that in case of very rough electrodes (*e.g.* containing deep scratches in the surface) there might be a gradual transition from the planar semi-infinite diffusion mode towards a finite diffusion domain response since the relative contribution of the reaction inside of the confined space of a scratch will increase. Therefore, a increasing depth of a rough surface profile can lead to a gradual transition from roughness to porosity.

Since the theory of cyclic voltammetry in finite diffusion domains [9–12] already suggests that (independent of the electrode geometry) the shape of the current response is largely dependent on the time-scale of the experiment, similar behavior may be expected for rough surfaces. Consequently, it has to be expected that the alleged increase in electrode kinetics cannot be described by a linear scaling factor derived from the area-ratio but will follow a more complicated function instead.

For unraveling the intricate entanglement of electrode kinetics and mass-transfer towards a rough electrode, we decided to employ the so called *master-equation* approach which is well known in the context of convolutive modeling and which was introduced in the work of Oldham [13–15]. The initial idea was to mathematically pinpoint the influence of electrode roughness in a semi-analytical framework. It should be noted that this cannot be done via classical digital simulation algorithms which are popular in the context of CV simulation, as these provide a numerical solution for the CV curve, but no (semi)analytical formalism.

The main challenge for convolutive modeling is, however, that it requires for a function which achieves a time-domain parametriza-tion of the mass-transfer at the electrode and the diffusion space under investigation. For highly symmetrical configurations, these time-dependent mass-transfer functions are known as analytical expressions or in the form of approximate solutions in the literature (*e.g.* for planar electrodes [9,16], cylindrical electrodes [17,18] and spherical electrodes [12]). Moreover, algorithms for pointwise evaluation of the mass-transfer phenomena based on numerical Laplace transformation inversion techniques have been proposed [19–21]. These do only require Laplace-domain solutions for the mass-transfer functions, which are generally much simpler to assess. Nevertheless, all of these ideas require well-defined and highly symmetrical electrodes and rely on one-dimensional diffusion models only. In case of a rough electrode surface,

the diffusion is, however, inherently random and needs to be described in three spatial dimensions.

An approach for using convolutive modeling at random electrode structures was presented in one of our previous publications [22]. There we proposed a strategy for simulating CV in the confined space of a porous (carbon felt) electrode. This strategy is adopted here and resulted in the modified digital-simulation–deconvolution–convolution (DSDC) algorithm presented herein.

Starting from the original DSDC-algorithm, the digital simulation step (DS) is tailored for computations on rough surfaces. This is achieved by employing an adaptive numerical resolution and by implementing an arbitrarily incremented spatial grid perpendicular to the macroscop-ically planar electrode surface for using computational power more efficiently. Additionally, the deconvolution step, required for extracting the mass-transfer function of the rough surface under investigation, is significantly improved. This procedure, which has been a recursive computation in the original algorithm, is replaced by a three-step sequence. In particular: (I) a numerical Laplace transformation of the flux obtained from the DS-step is followed by (II) a Laplace-domain integration before (III) the mass-transfer function of the rough electrode structure is finally obtained by a numerical inversion of Laplace trans-formation based on the Gaver–Stehfest [23] algorithm. Subsequently, CV simulation is performed by means of classical convolutive modeling to investigate the effects of electrode roughness. It is shown that the voltammetric profile of an electrochemically reversible reaction is independent from the electrode roughness on common experimental timescales. However, for electrochemically quasi-reversible (or irre-versible) reactions an alleged increase of the kinetics is obtained. At very high potential sweep-rates, the voltammetric curve is significantly distorted, showing features of a finite diffusion domain similar to porous electrodes. Both of these findings are quantitatively explained in terms of a convolutive *master-equation*, invoking the parameter electrode roughness into the semianalytical framework of convolutive modeling.

2. State of the art

Before outlining the modifications which have been introduced into the digital-simulation–deconvolution–convolution (DSDC) algorithm in detail, the original steps [22] of this procedure are outlined here. Ini-tially, the DSDC-algorithm was developed for the real-space simulation of electroanalytical experiments at macroporous electrodes (*e.g.* carbon felts). It consisted of the following successive steps:

Digital simulation (DS)

(I) The diffusion domain of the porous structure is discretized into a spatial grid of the same resolution in the x, y and z direction inside and outside of the electrode.

(II) Cottrellian conditions (zero concentration at $t > 0$) at the electrode/ electrolyte boundaries and a no-flux constraint (Neumann-boundary) at the opposite end of the diffusion domain are imposed.

(III) A sigmoidally incremented time-grid is introduced whose initial step-size is chosen to be $\Delta t_0 = \lambda \Delta x^2/D$, with D being the diffusion coefficient, Δx being the spatial increment and $\lambda = 0.1$ being the dimension-less numerical resolution ensuring convergence. Δt is allowed to increase up to a threshold $\Delta t_{\max}$. The rate of increase and the threshold value have to be determined via numerical experimentation though.

(IV) Upon definition of the space-grid and time-grid, the diffusion problem is solved by the Douglas–Gunn modification of the Crank–Nicolson scheme, an unconditionally stable finite difference method. This requires as many iterations until the desired timescale of the experiment $t_{\text{final}} = \sum \Delta t$ is reached.

(V) The flux at the electrode/electrolyte boundary is computed in each and every time-iteration according to Fick´s first law in three spatial dimensions.

(VI) The non-convergent region of the flux at low times t is masked and replaced by the values from semi-infinite diffusion. The transition region is interpolated. This defines the Cottrellian flux of the three-dimensional (porous) electrode structure.

Deconvolution (D)

(I) Based on the Cottrellian flux of the porous electrode structure which was computed in the DS-step, the mass transfer function $M(t)$ is extracted in a numerical deconvolution step. This procedure is recursive and requires an exceptionally small time-incrementation. Despite from being sufficiently accurate, this calculation is, unfortunately, inefficient from a computational perspective.

Convolution (C)

(I) Once the mass-transfer function is obtained, classical convolutive modeling can be employed for CV simulation, *i.e.* the master-equation approach — referred to as a semi-analytical solution — can be used.

3. Theory

Prior to adopting the DSDC-algorithm for the simulation of CV at rough interfaces, it is worth to consider qualitative differences between electrode roughness and electrode porosity. For a porous medium, mass-transfer originates mainly from the electrolyte encapsulated inside the electrode structure. In contrast, for a rough electrode the main mode of diffusive mass transfer is perpendicular to the macroscopically flat surface. This qualitative remark can be used to significantly reduce the computational effort of the digital simulation step of the DSDC-algorithm as outlined in the following.

3.1. Digital simulation

In analogy to the previous version of the DSDC-algorithm [22] the cartesian version of the three-dimensional diffusion equation (Eq. (1)) is used as starting point.

$$\frac{\partial c(x,y,z,t)}{\partial t} = D \left(\frac{\partial^2 c(x,y,z,t)}{\partial x^2} + \frac{\partial^2 c(x,y,z,t)}{\partial y^2} + \frac{\partial^2 c(x,y,z,t)}{\partial z^2} \right) \quad (1)$$

Defining that the rough interface is predominantly located in the xy-plane, and considering that concentration changes in the bulk of the electrolyte are minor, Eq. (1) can be discretized with a progressively

expanding incrementation along the z-direction and a homogeneous incrementation along the x and y directions. A fully homogeneous incrementation (along the x, y and z directions) is only required for the part where the electrode is actually rough. For convenience, an exponentially expanding discretization of the z-direction may be chosen for the electrolyte, which is illustrated in Fig. 2. Introducing the counting of spatial grid-points along the x, y and z directions with iterators i, j and k, the step-size along the z-direction is defined by

$$\Delta z_{k_{\text{electrolyte}}} = \Delta z_{k_{\text{last,electrode}}} \exp\left(\epsilon \left(k - k_{\text{last}}\right)\right), \quad (2)$$

where ϵ is the stretching parameter of the spatial increments along the z-direction inside of the electrolyte which needs to be determined by numerical experimentation.

The finite difference approximation of Eq. (1) then takes the form of

$$\frac{c_{i,j,k,t+\Delta t} - c_{i,j,k,t}}{\Delta t} \approx D \left(\frac{c_{i+1,j,k,t} - 2c_{i,j,k,t} + c_{i-1,j,k,t}}{\Delta x^2} \right.$$
$$+ \frac{c_{i,j+1,k,t} - 2c_{i,j,k,t} + c_{i,j-1,k,t}}{\Delta y^2} \qquad (3)$$
$$\left. + \alpha_k c_{i,j,k-1,t} + \beta_k c_{i,j,k,t} + \gamma_k c_{i,j,k+1,t} \right),$$

where the variable of time t was discretized into increments of Δt and x and y in increments of Δx and Δy and the arbitrary spacing along the z-direction was implemented in terms of finite differences by considering position-dependent coefficients α_k, β_k and γ_k. The exact method for computing these coefficients is introduced in Ref. [24] and, for the sake of completeness, outlined in Appendix A.1 of Appendix.

In Eq. (3) it is worth to note that the left hand side (*i.e.* the derivative with respect to time) has first order accuracy, whereas the spatial derivatives on the right hand side are second order approximations. Second order accuracy in space and time can be achieved by introducing the unconditionally stable, semi-implicit Crank–Nicolson scheme which was pioneered in the context of electrochemistry by Heinze and Störzbach [25,26]. This procedure averages the concentration values at a given time-instance t with the yet unknown concentration values at $t + \Delta t$. Setting $\lambda = D\Delta t/\Delta x^2$, $\tilde{\alpha}_k = \alpha_k D\Delta t$, $\tilde{\beta}_k = \beta_k D\Delta t$, $\tilde{\gamma}_k = \gamma_k D\Delta t$ and taking the advantage of $\Delta x = \Delta y$, the Crank–Nicolson modification of Eq. (3) gives

$$c_{i,j,k,t+\Delta t} - c_{i,j,k,t} \approx \frac{\lambda}{2} \left(c^p_{i+2,j+1,k+1,t} - 2c^p_{i+1,j+1,k+1,t} + c^p_{i,j+1,k+1,t} \right.$$
$$+ c^p_{i+1,j+2,k+1,t} - 2c^p_{i+1,j+1,k+1,t} + c^p_{i+1,j,k+1,t}$$
$$+ c^p_{i+2,j+1,k+1,t+\Delta t} - 2c^p_{i+1,j+1,k+1,t+\Delta t} + c^p_{i,j+1,k+1,t+\Delta t}$$
$$\left. + c^p_{i+1,j+2,k+1,t+\Delta t} - 2c^p_{i+1,j+1,k+1,t+\Delta t} + c^p_{i+1,j,k+1,t+\Delta t} \right) \quad (4)$$
$$+ \frac{1}{2} \left[\tilde{\alpha}_k c^p_{i+1,j+1,k,t} + \tilde{\beta}_k c^p_{i+1,j+1,k+1,t} + \tilde{\gamma}_k c^p_{i+1,j+1,k+2,t} \right.$$
$$+ \tilde{\alpha}_k c^p_{i+1,j+1,k,t+\Delta t} + \tilde{\beta}_k c^p_{i+1,j+1,k+1,t+\Delta t}$$
$$\left. + \tilde{\gamma}_k c^p_{i+1,j+1,k+2,t+\Delta t} \right],$$

where the values of c have been replaced by c^p. This modification is required since the points at $i = -1$, $j = -1$, $k = -1$, $i = i_{\max} + 1$, $j = j_{\max}+1$, and $k = k_{\max}+1$ in Eq. (3) lie outside of the actual sample space. Since these points are, however, mandatory for the computation they can be implicitly defined by assuming a no-flux boundary. Technically, this is done by a procedure called *padding*. This introduces a set of 'ghost points' with the same concentration value as their internally adjacent grid-points. As a consequence of padding, the counting of spatial grid points is shifted according to $c^p_{i+1,j+1,k+1} = c_{i,j,k}$.

As outlined in our previous publication [22], a direct solution of Eq. (4) is impractical. This is essentially caused by the fact that it requires the processing of large heptadiagonal matrices. A more sophisticated approach is to introduce the Douglas–Gunn modification [27] of the Crank–Nicolson scheme which is known from the context of heat-conduction [28]. This procedure splits each time-iteration (*i.e.* from
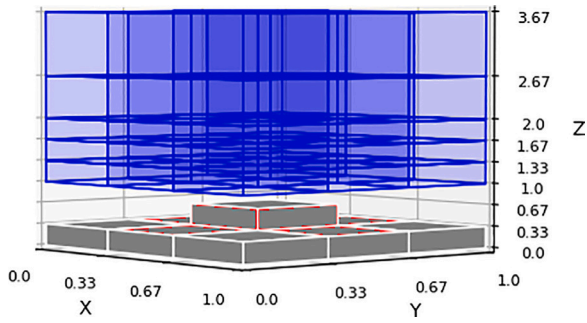
Fig. 2. Illustration of an exponentially expanding electrolyte grid (blue) on top of a homogeneously incremented electrode grid on top of a rough electrode surface. The roughness of the electrode is implied by one elevated voxel in the center of the electrode.

$c_{i,j,k,t} \rightarrow c_{i,j,k,t+\Delta t}$) into three sub-steps which are alternatingly implicit in the x, y and z-directions. This allows a successive processing of the entire dataset in the form of smaller (columnar) sub-systems while preserving the second order accuracy of the original algorithm. These sub-systems can be represented by tridiagonal matrix–vector multiplications and solved efficiently as set of linear equations with the Thomas algorithm [29]. Moreover, they are independent from one-another which allows parallel processing. Since Eq. (4) is defined on an arbitrarily spaced grid along the z-direction, the classical Douglas–Gunn algorithm (*e.g.* outlined in Ref. [28]) needs to be modified and matched with the constraint of a zero-concentration at each electrode/electrolyte boundary at $t > 0$ (*i.e.* a Cottrellian potential step experiment). This requires the inclusion of internal boundary points and adaptive grid coefficients. For the three sub-steps of the Douglas–Gunn algorithm this gives:

Step 1/3

The first sub-step is defined to be implicit in x and explicit in y and z. It requires a computation of the auxiliary concentrations according to

$$
\begin{aligned}
c^*_{i,j,k,t+\Delta t/3} = \Big[&\lambda \big[c^p_{i,j+1,k+1,t} + c^p_{i+2,j+1,k+1,t} + 2\big(c^p_{i+1,j,k+1,t} + c^p_{i+1,j+2,k+1,t}\big) \\
&- 6c^p_{i+1,j+1,k+1,t} \big] + 2 \big[\tilde{\alpha}_k c^p_{i+1,j+1,k,t} + (1+\tilde{\beta}_k)c^p_{i+1,j+1,k+1,t} \\
&+ \tilde{\gamma}_k c^p_{i+1,j+1,k+2,t} \big] \Big] b_{i,j,k},
\end{aligned}
$$
(5)

where $b_{i,j,k} = c_{i,j,k,t=0}/c_{\text{bulk}}$. The concentrations at time-instance $t+\Delta t/3$ are then related to the auxiliary concentrations according to

$$
\underline{\underline{M}}_{j,k,t+\Delta t/3}\ \underline{c}_{j,k,t+\Delta t/3} = \underline{c}^*_{j,k,t+\Delta t/3},
$$
(6)

where $\underline{c}_{j,k,t+\Delta t/3}$ and $\underline{c}^*_{j,k,t+\Delta t/3}$ are columnar vectors along the x-direction at positions j and k of the yz-plane. The matrix $\underline{\underline{M}}_{j,k,t+\Delta t/3}$ contains all internal boundaries and is defined by

$$
\underline{\underline{M}}_{j,k,t+\Delta t/3} = \begin{pmatrix} d_{0,j,k} & -\lambda\, b_{0,j,k} & \\ -\lambda\, b_{i=m,j,k} & d_{i=m,j,k} & -\lambda\, b_{i=m,j,k} \\ & -\lambda\, b_{i_{\max},j,k} & d_{i_{\max},j,k} \end{pmatrix}
$$
(7)

where $d_{0,j,k} = (2+\lambda)b_{0,j,k} + b^*_{0,j,k}$ and $d_{i=m,j,k} = 2(1+\lambda)b_{i=m,j,k} + b^*_{i=m,j,k}$ and $d_{i_{\max},j,k} = (2+\lambda)b_{i_{\max},j,k} + b^*_{i_{\max},j,k}$ and $b^*_{i,j,k} = (b_{i,j,k}-1)^2$ and m is the line-index of matrix $\underline{\underline{M}}$.

Step 2/3:

Subsequently to computing the values of $c_{i,j,k,t+\Delta t/3}$, the second sub-step in time is defined to be implicit in y and explicit in x and z. Previously computed values of $c_{i,j,k,t+\Delta t/3}$ are padded and invoked

according to

$$
\begin{aligned}
c^*_{i,j,k,t+2\Delta t/3} = \Big[&\lambda \big[c^p_{i,j+1,k+1,t} + c^p_{i+2,j+1,k+1,t} + c^p_{i+1,j,k+1,t} + c^p_{i+1,j+2,k+1,t} \\
&- 4c^p_{i+1,j+1,k+1,t} + c^p_{i,j+1,k+1,t+\Delta t/3} - 2c^p_{i+1,j+1,k+1,t+\Delta t/3} \\
&+ c^p_{i+2,j+1,k+1,t+\Delta t/3} \big] + 2 \big[\tilde{\alpha}_k c^p_{i+1,j+1,k,t} + (1+\tilde{\beta}_k)c^p_{i+1,j+1,k+1,t} \\
&+ \tilde{\gamma}_k c^p_{i+1,j+1,k+2,t} \big] \Big] b_{i,j,k}.
\end{aligned}
$$
(8)

The concentrations at time-instance $t+2\Delta t/3$ are then related to the auxiliary concentrations according to

$$
\underline{\underline{M}}_{i,k,t+\Delta 2t/3}\ \underline{c}_{i,k,t+\Delta 2t/3} = \underline{c}^*_{i,k,t+\Delta 2t/3}.
$$
(9)

In analogy to the first sub-step, the concentrations $\underline{c}_{i,k,t+2\Delta t/3}$ and $\underline{c}^*_{i,k,t+2\Delta t/3}$ are columnar vectors along the y-direction at positions i and k of the xz-plane. The matrix $\underline{\underline{M}}_{i,k,t+2\Delta t/3}$ contains all internal boundaries and is defined by

$$
\underline{\underline{M}}_{i,k,t+2\Delta t/3} = \begin{pmatrix} d_{i,0,k} & -\lambda\, b_{i,0,k} & \\ -\lambda\, b_{i,j=m,k} & d_{i,j=m,k} & -\lambda\, b_{i,j=m,k} \\ & -\lambda\, b_{i,j_{\max},k} & d_{i,j_{\max},k} \end{pmatrix}
$$
(10)

where $d_{i,0,k} = (2+\lambda)b_{i,0,k} + b^*_{i,0,k}$ and $d_{i,j=m,k} = 2(1+\lambda)b_{i,j=m,k} + b^*_{i,j=m,k}$ and $d_{i,j_{\max},k} = (2+\lambda)b^*_{i,j_{\max},k} + b_{i,j_{\max},k}$.

Step 3/3:

The third sub-step in time is defined to be implicit in z and explicit in x and y. It requires the inclusion of the previously computed values of $c_{i,j,k,t+\Delta t/3}$ and $c_{i,j,k,t+2\Delta t/3}$. The intermediate concentrations are then defined by

$$
\begin{aligned}
c^*_{i,j,k,t+\Delta t} = \Big[&\lambda \big[c^p_{i,j+1,k+1,t} + c^p_{i+2,j+1,k+1,t} + c^p_{i+1,j,k+1,t} + c^p_{i+1,j+2,k+1,t} \\
&- 4c^p_{i+1,j+1,k+1,t} + c^p_{i,j+1,k+1,t+\Delta t/3} - 2c^p_{i+1,j+1,k+1,t+\Delta t/3} \\
&+ c^p_{i+2,j+1,k+1,t+\Delta t/3} + c^p_{i+1,j+1,k+2\Delta t/3} - 2c^p_{i+1,j+1,k+1,t+2\Delta t/3} \\
&+ c^p_{i+1,j+2,k+1,t+2\Delta t/3} \big] + \tilde{\alpha}_k c^p_{i+1,j+1,k,t} + (2+\tilde{\beta}_k)c^p_{i+1,j+1,k+1,t} \\
&+ \tilde{\gamma}_k c^p_{i+1,j+1,k+2,t} \Big] b_{i,j,k},
\end{aligned}
$$
(11)

and related to the concentrations according to

$$
\underline{\underline{M}}_{i,j,t+\Delta t}\ \underline{c}_{i,j,t+\Delta t} = \underline{c}^*_{i,j,t+\Delta t},
$$
(12)

where $\underline{c}_{i,j,t+\Delta t}$ and $\underline{c}^*_{i,j,t+\Delta t}$ are column vectors along the z-direction standing on the xy-plane. The matrix $\underline{\underline{M}}_{i,j,t+\Delta t}$ requires a notation slightly different from steps 1/3 and 2/3, since the z-direction contains the expanding spatial grid. It is defined by

$$
\underline{\underline{M}}_{i,j,t+\Delta t} = \begin{pmatrix} d_{i,j,0} & -\tilde{\gamma}_0\, b_{i,j,0} & \\ -\tilde{\alpha}_k\, b_{i,j,k=m} & d_{i,j,k=m} & -\tilde{\gamma}_k\, b_{i,j,k=m} \\ & -\tilde{\alpha}_k\, b_{i,j,k_{\max}} & d_{i,j,k=k_{\max}} \\ & & \end{pmatrix}
$$
(13)

where the entries of the main diagonal are $d_{i,j,0} = (2-\tilde{\alpha}_0-\tilde{\beta}_0)b_{i,j,0} + b^*_{i,j,0}$ and $d_{i,j,k=m} = (2-\tilde{\beta}_k)b_{i,j,k=m} + b^*_{i,j,k=m}$ and $d_{i,j,k=k_{\max}} = (2-\tilde{\beta}_{k_{\max}} - \tilde{\gamma}_{k_{\max}})b_{i,j,k_{\max}} + b^*_{i,j,k_{\max}}$.

3.1.1. Computing the cumulated flux-response

The flux at each point of the three-dimensional sample space can be computed at time t from Fick's first law as

$$
J(x,y,z,t) = -D\nabla c(x,y,z,t).
$$
(14)

For electrochemical applications, however, only the cumulated flux at the electrode/electrolyte interface is important, as this quantity is directly proportional to the Faradaic current. Since the spatial resolution inside of the rough part of the electrode is set to be equal along the x, y and z-directions with increment $\Delta x = \Delta y = \Delta z = h$, Eq. (14) can be numerically approximated by using the padded versions of the

concentrations at the respective time. The cumulated flux at a given time instance is then obtained as

$$
\begin{aligned}
J(t) \approx -\frac{D}{h} \sum_{i,j,k} \Big[& \, c^p_{i,j+1,k+1,t} + c^p_{i+2,j+1,k+1,t} + c^p_{i+1,j,k+1,t} \\
& + c^p_{i+1,j+2,k+1,t} + c^p_{i+1,j+1,k,t} + c^p_{i+1,j+1,k+2,t} \\
& - 6c^p_{i+1,j+1,k+1,t} \Big] b^*_{i,j,k,t}.
\end{aligned}
\tag{15}
$$

Eq. (15) is finally used in each and every time before the sequence of Eqs. (5)–(13) is started. In this manner, the cumulated flux is obtained as a set of discrete points in time. Values at any other desired point in time need to be approximated — *e.g.* via spline interpolation.

3.2. Deconvolution and extraction of the mass-transfer function

For most electroanalytical experiments, the flux computed by Eq. (15) is not sufficient. This is essentially caused by the fact that it was generated by assuming a Cottrellian potential step experiment, where the concentration at each electrode/electrolyte interface is forced to be zero at $t > 0$. For this reason, it excludes all effects from electrode kinetics by definition. Simultaneously it does, however, contain the entire information of the diffusive mass transfer of the electrode under investigation. In our previous work [18], we derived the general connection between the mass-transfer function and the normalized flux of a Cottrellian potential step experiment by means of Laplace transformation techniques. From this work it follows that the normalized cumulated flux can be expressed as

$$
f(t) = \frac{J(t)}{c_{\text{bulk}} A_{\text{rough}} \sqrt{D}}.
\tag{16}
$$

The normalized flux and the mass-transfer-function $m(t)$ are connected by Laplace transformation and its inversion. Firstly,

$$
f(t) = \mathcal{L}^{-1} \left\{ \frac{1}{s \overline{m}(s)} \right\}(t),
\tag{17}
$$

where $\overline{m}(s)$ is the Laplace transformation of $m(t)$ with s being the transformed variable related to the time t. Application of a Laplace transformation on both sides of Eq. (17) leads, after slight rearrangement, to

$$
\frac{1}{s} = \overline{f}(s) \overline{m}(s).
\tag{18}
$$

Taking the inverse Laplace transformations of both sides of Eq. (18), we arrive at

$$
1 = \int_0^t f(\tau) m(t-\tau) \, d\tau,
\tag{19}
$$

where the convolution theorem was used on the right hand side. Since $m(0) \to \infty$ [18], the integrand of Eq. (19) contains weak singularity at the upper integration limit. This singularity can be removed by an integration by parts, which gives

$$
1 = -M(t-\tau)f(\tau)\Big|^{\tau=t}_{\tau=0} + \int_{f(0)}^{f(t)} M(t-\tau) \, df(\tau),
\tag{20}
$$

where $M(t)$ is the antiderivative of $m(t)$. In previous works [22] we used a discretized version of Eq. (20) in a recursive algorithm to calculate the values of $M(t)$. Consideration of the boundary value $M(0) = 0$ and discretization of both, t and τ with identical increments ($t = u\Delta t$, $\tau = v\Delta t$, $v \le u$) gives

$$
1 \approx M(u\Delta)f(0) + \sum_{v=0}^{u-1} M((u-v)\Delta t)\big[f((v+1)\Delta t) - f(v\Delta t)\big].
\tag{21}
$$

A recursion relation for $M(u\Delta t)$ is obtained upon rearrangement

$$
M(u\Delta t) \approx \frac{1}{f(\Delta t)} \left[1 - \sum_{v=1}^{u-1} M((u-v)\Delta t)\big[f((v+1)\Delta t) - f(v\Delta t)\big] \right].
\tag{22}
$$

Despite the fact that Eq. (22) can be used to calculate $M(t)$ with reasonable accuracy by choosing Δt sufficiently small, this approach is

not too practical. This is essentially caused by the fact that the recursive sum includes an excessive amount of terms if Δt decreases. In fact, this was the motivation for the approach presented in the following.

Alternatively to applying inverse Laplace transformation on Eq. (18) by the convolution theorem, one may convert it first into an equation for $\overline{M}(s)$ — the Laplace transformed antiderivative $M(t)$ of the mass-transfer function $m(t)$. An integration in the time domain corresponds to a division by the transformed variable (here s) in the Laplace-domain. Therefore, we obtain

$$
\overline{M}(s) = \frac{1}{s^2 \overline{f}(s)}.
\tag{23}
$$

The path to $M(t)$ is now reduced to (I) finding the Laplace transform $\overline{f}(s)$ and (II) the subsequent inverse Laplace transformation of the right hand side of Eq. (23). Generally, the Laplace transformation of any $f(t)$ is defined as

$$
\overline{f}(s) = \int_0^\infty f(t) e^{-st} \, dt.
\tag{24}
$$

However, since the function f is, in our case, only available as a set of function values at $N+1$ equidistant, discrete points in time its Laplace transformation needs to be approximated. This is done by taking

$$
\begin{aligned}
\overline{f}(s) \approx \frac{1}{2} \Big[& \, f(t_0) e^{-st_0}(t_1 - t_0) + f(t_N) e^{-st_N}(t_N - t_{N-1}) \\
& + \sum_{w=1}^{N-1} f(t_w) e^{-st_w}(t_{w+1} - t_{w-1}) \Big]
\end{aligned}
\tag{25}
$$

It is, however, important to underline that a *true* Laplace transform of the function $f(t)$ requires an integration over the entire t-axis. Hence, in Eq. (25) t_0 has to be chosen sufficiently small and t_N sufficiently large to minimize truncation errors. Practically, this is problematic, since an exceptionally high resolution of the time-grid and a very large maximum-time would be required. Intuitively, this translates to an excessive amount of time-steps in the preceding digital simulation part of the algorithm. A practical workaround for this is given in Section 3.4.

3.2.1. Laplace-domain processing and Gaver–Stehfest inversion

With a table of values for $\overline{f}(s)$ at hand, the corresponding values of $\overline{M}(s)$ are readily obtained from Eq. (23). The most crucial step is then the inverse Laplace transformation of $\overline{M}(s)$ in order to get $M(t)$.

Since $\overline{M}(s)$ is obtained as a set of discrete points along the real-axis in s-space only, neither the complex inversion formula, nor its complex approximations (*i.e.* the Talbot-method [30] and its more recent relatives [31,32] we have used in previous works [21]) can be employed. Fortunately, however, there is a *real-value-only* approximation of the complex inversion formula — the so called Gaver–Stehfest inversion [23]. This formula has been introduced in the context of electrochemistry by Montella [19,20,33]. Generally, the Gaver–Stehfest inversion is restricted to functions which do not possess oscillatory behavior in the time domain. Fortunately, the diffusion process of a Cottrellian potential step can be expected to have exactly this behavior as the current decays smoothly. Using the Gaver–Stehfest inversion formula explicitly on Eq. (23) gives

$$
M(t) \approx \frac{\ln(2)}{t} \sum_{k=1}^{2N} a_k(N) \left[\frac{k^2 \ln(2)^2}{t^2} \cdot \overline{f}\left(\frac{k \ln(2)}{t}\right) \right]^{-1},
\tag{26}
$$

where the coefficients $a_k(N)$ are defined in terms of binominal coefficients as

$$
a_k(N) = \frac{(-1)^{N+k}}{N!} \sum_{j=\lfloor (k+1)/2 \rfloor}^{\min(k,N)} j^{N+1} \binom{N}{j} \binom{2j}{j} \binom{j}{k-j}.
\tag{27}
$$

Since Eq. (26) requires the values of $\overline{f}(s)$ to be defined at points $s_k = k \ln(2)/t$ ($k = 1, \dots, 2N$), interpolation between values at the previously defined set of s-values is usually required prior to numerical inversion. Finally, Eq. (26) can be used to evaluate $M(t)$ at the desired time

instances required for simulating the actual electroanalytical experiments. This is, however, not too practical either. A faster solution is to evaluate $M(t)$ on a set of logarithmically spaced points in time and to interpolate to the actually required time instances.

3.3. Convoluting electrode kinetics with the mass-transfer function

Once the function $M(t)$ has been determined, the well-known *master equation* approach of convolutive modeling can be used to compute the voltammetric current-response of any electrode at any degree of reversibility. In the course of this paper, the general solution for a single-step electron transfer is used for the sake of simplicity, *i.e.* the current can be computed exploiting the following approximation

$$I(m\Delta t) \approx \frac{nFA_{\text{rough}}c_{\text{red,bulk}}\sqrt{D} - \left[1 + e^{-\xi(m\Delta t)}\right] \cdot S_{I,M}}{\dfrac{\sqrt{D}\,e^{-\alpha\xi(m\Delta t)}}{k^0} + M(\Delta t)\left[1 + e^{-\xi(m\Delta t)}\right]}. \tag{28}$$

In Eq. (28), S is defined by

$$S_{I,M} = \sum_{j=1}^{m-1} I(j\Delta t)\left[M((m-j+1)\Delta t) - M((m-j)\Delta t)\right]. \tag{29}$$

and $\xi(t)$ by

$$\xi(t) = \frac{nF}{RT}\left[E(t) - E^0\right]. \tag{30}$$

The parameters α and k^0 are the electron transfer coefficient and the heterogeneous rate constant of the electrochemical reaction, respectively. It should be underlined that Eq. (28) excludes optional first-order chemical reactions, Ohmic and capacitive distortion, and finite kinetics by definition. These could be, however, included in a straightforward manner by consulting the respective Refs. [21,22,34, 35].

3.4. Adaptive resolution for the digital simulation step

Introducing an adaptive numerical resolution — not to be confused with the expanding z-grid introduced earlier — into the digital simulation step is practically motivated by four particular considerations.

(I) From our previous publication it is known that in the limit of $t \to 0$, any diffusion towards an arbitrarily shaped surface will behave in a planar semi-infinite fashion. Consequently, the normalized flux is obtained from the Cottrell-equation as

$$f(t) = \frac{I_{\text{Cott}}(t)}{nFAc_{\text{bluk}}\sqrt{D}} = \frac{1}{\sqrt{\pi t}}. \tag{31}$$

This implies the existence of a low-time threshold below which the simulations may be stopped and normalized flux extrapolated by Eq. (31). Finding the particular low-time cutoff is, however, challenging for the following reasons. Since the computations of the DS-step are performed on a spatially discretized diffusion domain, any electrolyte-point adjacent to more than one reactive site (*i.e.* any concave edge or corner) will introduce a remainder where diffusion cannot be described as semi-infinite (cf. Fig. 3). Though the relative contribution of this remainder can be reduced by increasing the spatial resolution during the simulations (cf. in Fig. 3 (A)-(C)), it cannot be avoided completely. Simultaneously, a higher spatial resolution will tremendously increase the number of spatial grid-points and thus the computational demand required for the simulations. The workaround used in this paper is to increase the spatial resolution, until the numerically computed flux reaches a defined similarity to the analytical solution of the planar semi-infinite case and to interpolate a certain time-frame between analytical solution and the numerically computed result.

(II) Considering that a planar electrode is exposed to an electrolyte medium one has to pose the question at which timescale the diffusion zone will reach the opposite border of the electrochemical cell. At this point in time, mass-transfer cannot be expected to be semi-infinite anymore and externally-finite diffusion domain effects will progressively dominate. For an ideally planar electrode the time dependent concentration profile is given in terms of the following analytical expression [36]

$$\frac{c(z,t)}{c_{\text{bulk}}} = \text{erf}\left(\frac{z}{2\sqrt{Dt}}\right), \tag{32}$$

where erf is the error function and z the direction perpendicular to the electrode surface. This expression can be rearranged to find the point in space at which the concentration ratio $\phi(z,t) = c(z,t)/c_{\text{bulk}}$ will take on a certain value at a given time. Defining $t_{\max}$ to be the maximum time of the experiment to be computed, one can find

$$z_{\max} = 2\sqrt{Dt_{\max}}\,\text{erfinv}\left(\phi(z_{\max}, t_{\max})\right). \tag{33}$$

This is of particular relevance for the computations, as it suggests the existence of a minimum sample volume required for ensuring semi-infinite diffusion conditions. While smaller volumina will result in boundary-errors, larger volumina are computationally wasteful.

(III) The dimension-less parameter $\lambda = D\Delta t/\Delta x^2$, controlling the numerical accuracy of the DS-step would be significantly affected, if the spatial resolution of the electrode grid is increased as suggested in point (I). Since this is not desired, the λ-values may be preserved by refining the time-grid by factor N^2 when the spatial coordinates are refined by factor N. Despite the fact that this excessive refinement of the time-grid will perfectly match the requirements[1] of Eq. (25), it is not too practical as an excessive amount of computation steps would be needed until experimentally relevant time-scales are reached. For this reason, the parameter λ may be allowed to expand in a well defined manner as a function of time, *i.e.* $\lambda \to \lambda(t)$, ensuring convergence of the simulations. In this work, the respective $\lambda(t)$-function is parametrized to meet the following requirements:

$$\lambda(t) = \begin{cases} \lambda_{\min} & t = t_{\min} \\ 0.5 & t = t_{\text{crit}} \\ \lambda_{\max} & t \to \infty \end{cases} \tag{34}$$

which can be achieved by setting

$$\lambda(t) = \lambda_{\min} + \frac{\left[\lambda_{\max} - \lambda_{\min}\right] g(t,\sigma)}{\left[\lambda_{\max} - \lambda_{\min}\right] + g(t,\sigma)}. \tag{35}$$

where

$$g(t,\sigma) = -\lambda_{\min}\left[1 - \exp\left(\sigma(t - t_{\min})\right)\right]. \tag{36}$$

From Eqs. (35) and (36) it directly follows that Eq. (34) is fulfilled for $t = t_{\min}$ and $t \to \infty$, leaving the point where $\lambda = 0.5$ to be defined. Imposing the constraint of $\lambda = 0.5$ on Eqs. (35) and (36), one can find

$$\sigma = \frac{1}{t_{\text{crit}} - t_{\min}}\ln\left(\frac{\lambda_{\min}\left(1 - \lambda_{\min}\right) - 0.5\,\lambda_{\max}}{\lambda_{\min}\left(0.5 - \lambda_{\max}\right)}\right), \tag{37}$$

where the only missing parameter is now t_{crit}. This particular point in time may be defined from a rearranged version of Eq. (33), such that

$$t_{\text{crit}} = \frac{1}{4D}\left[\frac{z_{\text{crit}}}{\text{erfinv}\left(\phi(z_{\text{crit}}, t_{\text{crit}})\right)}\right], \tag{38}$$

---

[1] An exceptionally narrow time-incrementation is required for rendering the first time-instance t_0 small enough for ensuring sufficient accuracy of the numerical Laplace transformation.
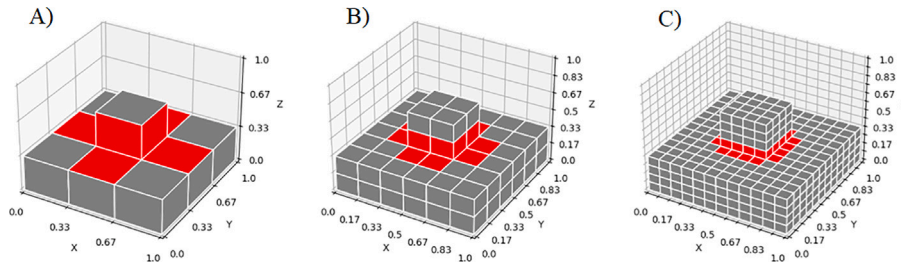
Fig. 3. Illustration of the *non-semi-infinite* part of the diffusion domain (highlighted in red). The relative contribution of this diffusive part is reduced by increasing the spatial refinement of the simulation as gradually shown from panel (A) to (C).
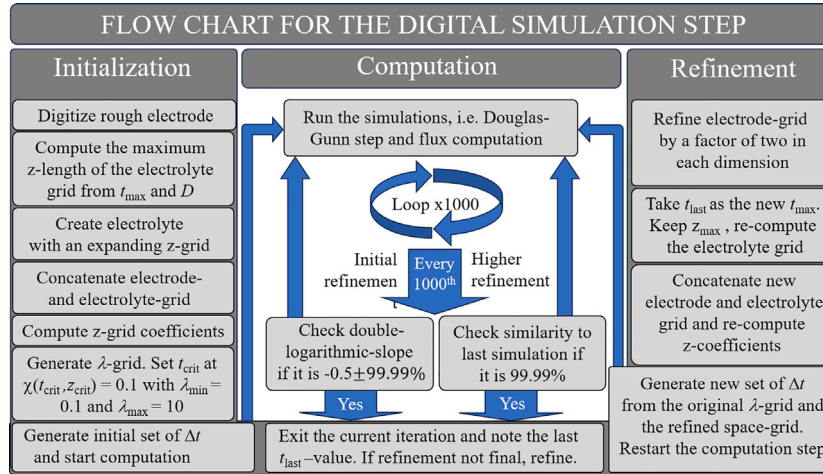

Fig. 4. Illustration of the process-flow of the digital simulation step, containing an initialization, a main-loop and a refinement step. Upon initialization of the electrode structure, the expanding electrolyte-grid, the λ-grid, and the Δt-grid, the main-loop (containing the Douglas–Gunn-algorithm and computation of the three-dimensional flux) is started. Every 1000 iterations, it is checked whether the simulations have converged to either the slope criterion (zeroth refinement step) or the similarity criterion (higher refinements). Once convergence is achieved, the spatial grid is refined by factor two, *i.e.* all spatial increments are subdivided into two segments. Based on this new space-grid, a refined time-grid is initialized before the next main-loop (with higher resolution) is started.

which shifts the problem from the variable of time to the variable of space. In this manner, t_{crit} can be defined by a particular distance from the electrode and the critical concentration ratio at this point. Providing an experimentally relevant measure one may choose this particular distance equivalent to the height of *deepest scratch* in the rough electrode.

(IV) Taking into account that diffusion has the inherent property of blurring, one may consider that, at a certain point in z-space and time, the influence of the surface-roughness can be neglected and mass-transfer will be dominated by the planar semi-infinite diffusion mode. Since the normalized flux will be, however, referred to the area A_{rough} one would have a dysbalance of normalized flux on a planar electrode and on a rough surface according to

$$\frac{I_{\mathrm{Cott}}(t)}{nFA_{\mathrm{rough}}c_{\mathrm{bulk}}\sqrt{D}} = f_{\mathrm{rough}}(t) \leq f(t) = \frac{I_{\mathrm{Cott}}(t)}{nFA_{\mathrm{geo}}c_{\mathrm{bulk}}\sqrt{D}}. \quad (39)$$

Therefore, an extrapolation similar to the low-time scenario is not possible. By taking the double-logarithmic derivative of Eq. (39), however, one may find the following important expression.

$$\left.\frac{d\log_{10}(f(t))}{d\log_{10}(t)}\right|_{t\geq t_{\mathrm{th}}} = \left.\frac{d\log_{10}\left(f_{\mathrm{rough}}(t)\right)}{d\log_{10}(t)}\right|_{t\geq t_{th}} = -0.5 \quad (40)$$

Using Eq. (40) one can define a threshold value where the double-logarithmic derivative of the normalized flux computed in the DS-step is equal to -0.5. Subsequently, one can linearly extrapolate the normalized flux at a slope of -0.5 on a double-logarithmic grid and therefore stop the actual computations.

These four important considerations have been used to derive the following process-flow for the DS-step, which is depicted in Fig. 4.

4. Results and discussion

Herein, we will make a conscious effort to bring our findings on the intricate interplay of electrode roughness, electrode kinetics and mass-transfer to the experimentalists community. Additionally, we will demonstrate how electrode roughness can be included into the context of convolutive modeling. However, before discussing the effects of electrode roughness in any depth, the modified DSDC-algorithm will be validated. All simulations in this paragraph have been performed with a diffusion coefficient of $D = 10^{-6}\,\mathrm{cm^2/s}$, an initial resolution of a 100 nm voxel size and similarity-thresholds of 99.99%. For different input parameters, the reader is referred to the supplementary material of this paper. There, we included scripts (written in Python 3 programming language) for performing simulations in analogy to this paper and a short hands-on guide to utilize them.

4.1. Validation of the algorithm with the ideally planar example

Validation of the modified DSDC-algorithm was done by performing the simulations for an ideally planar electrode in a three-dimensional diffusion space and comparing them against the normalized Cottrellian flux. Respective results are illustrated in Fig. 5. In Fig. 5 (A) and (B), the parametrization of the λ-grid and the normalized flux are depicted in double-logarithmic representations, respectively. Both sub-plots need to be read in parallel for illustrating the algorithm. Firstly, the λ-grid was initialized (Fig. 5-(A), black curve). The dashed horizontal lines in black illustrate the minimum $\lambda_{\mathrm{min}} = 0.1$, the maximum $\lambda_{\mathrm{max}} = 10$ and the point where $\lambda = 0.5$. The dashed vertical line in black represents the critical time t_{crit} defined in Eq. (34). The curves (a)–(f), depicted in gray, are the individual Δt-values computed from $\lambda(t)$,
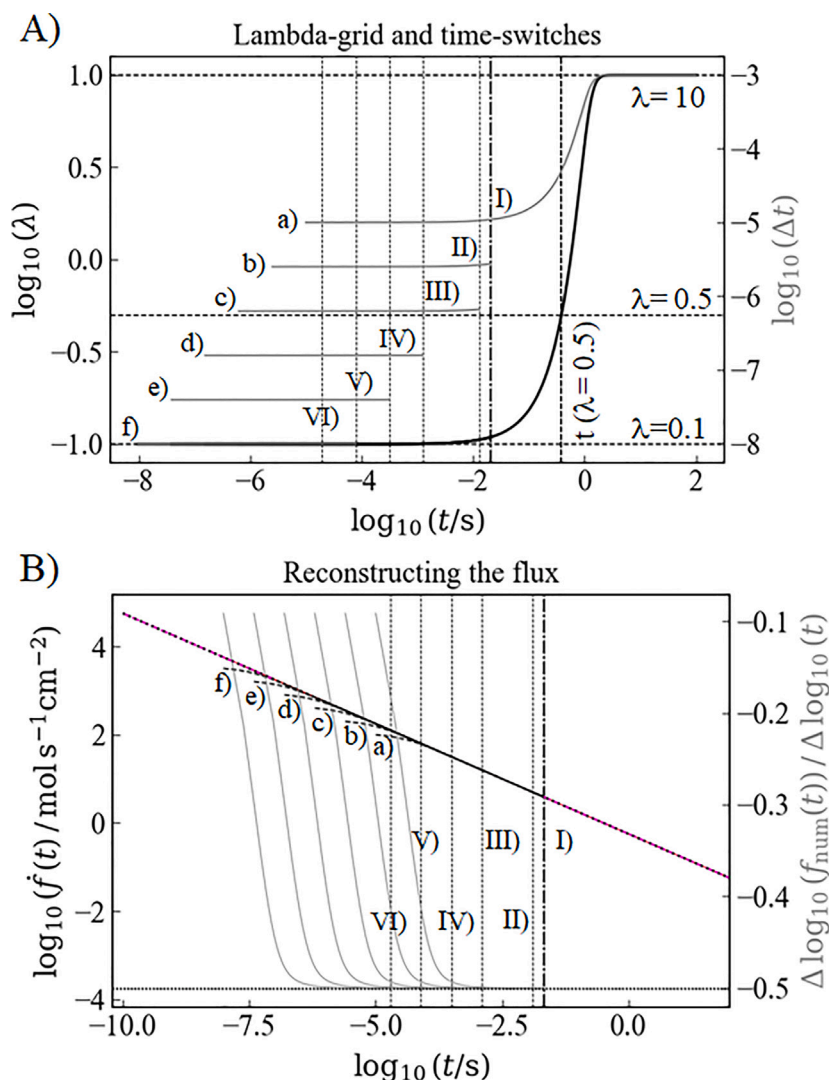
Fig. 5. Illustration of the DS-step for a planar electrode in a semi-infinite diffusion space. Panel (A) depicts the parametrized λ-grid and the individual Δt-grids and panel (B) the normalized flux-responses on a double logarithmic representation. Dashed lines mark $\lambda_{\min} = 0.1$, $\lambda_{\max} = 10$ as well as t_{crit}, where $\lambda = 0.5$. The dash-dotted vertical line (I) is the time at which the first simulation was stopped by the slope-criterion of 99.99% and the dotted vertices (II)–(VI) are the cutoff-times estimated by the similarity criterion of 99.99%. In panel (B), the curves (a) to (f) illustrate the normalized flux (dashed lines) or the double-logarithmic derivative of the normalized flux (gray curves). The line in pink is the analytical solution for the normalized flux in a double-logarithmic representation.

D and Δx^2 which have been used for the simulation. Computations at a certain resolution have been stopped for individual Δt-curves at the time-instances highlighted by (I) the dash-dotted vertical line (slope criterion) and (II)–(VI) the dotted vertical lines (similarity criterion). The same *cutoff-times* are depicted in Fig. 5-(B). This particular panel also shows the normalized flux (dotted curves (a)–(f) in black), its double-logarithmic derivative according to Eq. (40) (gray curves), and the analytical solution of the normalized flux of a planar electrode (pink curve) as reference. The actual computation started with the Δt-grid (a) of Fig. 5 (A) and resulted in the corresponding flux depicted by curve (a) in Fig. 5-(B). The simulation was terminated at time-instance (I) once the double-logarithmic derivative reached 99.99% of the slope of the semi-infinite diffusion (about $10^{-1.5}$ s). Larger times have been extrapolated linearly (dotted black curve superimposing the pink curve). After this, a refinement of the space-grid by factor two was performed. The maximum time of the next simulation was bounded to time (I). Using the initial λ-grid, the Δt-grid was refined to (b), as depicted in Fig. 5-(A).

Simulation (b) was explicitly performed until time-instance (II), where the flux achieved 99.99% of the previous computation. This procedure was repeated until iteration (f) with stopping-time (VI),

at a $2^5 = 32$-fold resolution of the initial stack-size. It can be seen that the normalized flux contains a non-convergent feature at low time-instances for all simulations which does, however, gradually shift towards lower time-scales, once the resolution increases. Additionally, it can be seen that all double-logarithmic derivatives converge to a value of -0.5 - as expected from Eq. (40). The last time before low-time interpolation was chosen to be 10^{-6} s. Values left to this time are generated by skipping one decade of time-incrementation before the current is set to be coincident with the planar semi-infinite solution. The remaining gap is closed by a cubic spline interpolation on the double-logarithmic grid. The normalized flux at time-scales larger than 10^{-6} s is extracted by using the results from the regions between points (V) to (I). Practically, this means using the flux-values of (f) between 10^{-6} s and point (VI), the flux values of (e) between points (VI) and (V), the flux values from (d) between points (V) and (IV) and so on. With this procedure, the normalized flux was finally obtained on a time-scale spanning from 10^{-20} s to 10^{20} s. This excessively lare time-window is required for investigating the convergence of the Laplace-domain processing and the modified deconvolution. In this context, the full-scale interpolation of the normalized flux was used on Eq. (25). Introducing a logarithmically spaced time-grid consisting of 160000 nodes (4000
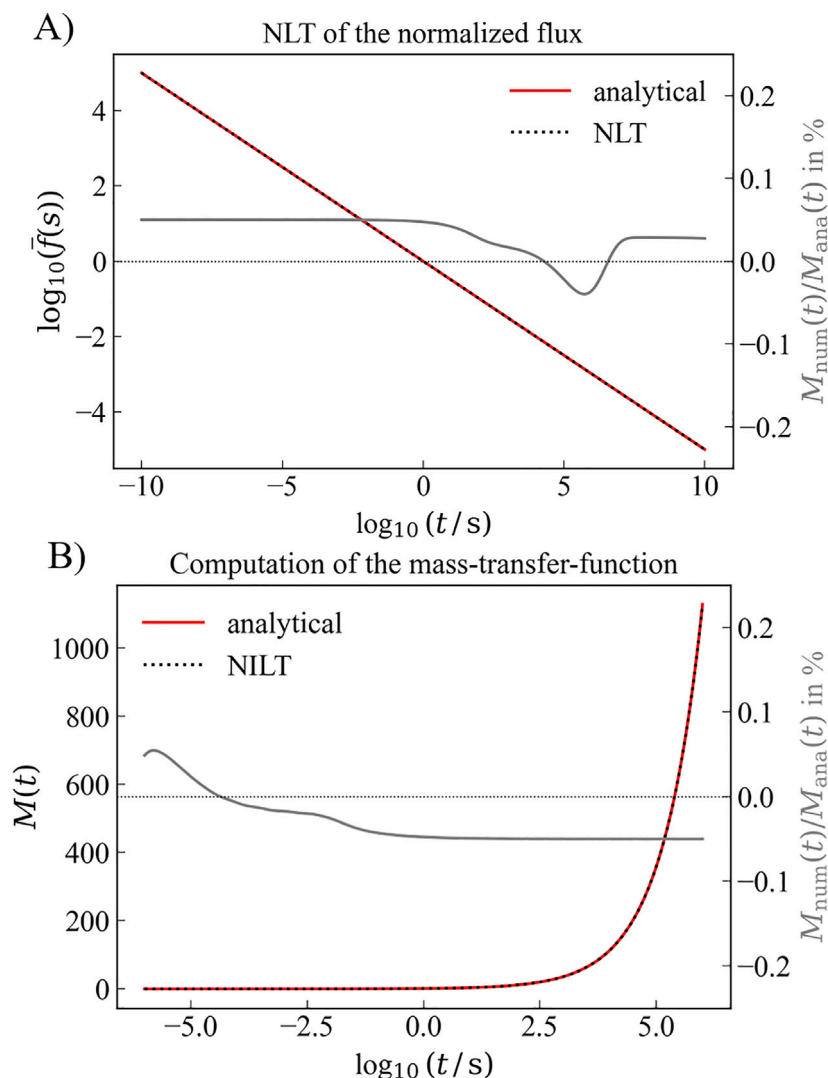
Fig. 6. Illustration of the deconvolution step for obtaining the mass-transfer function. Black dotted curves are the numerical result, curves in red the analytical solution and the gray traces are the relative deviation of analytical and numerical result. Panel (A) shows the numerical Laplace transformation of the normalized flux based on Eq. (25). Panel (B) depicts the Mass transfer function obtained from Laplace domain processing according to Eq. (23) and a subsequent numerical inverse Laplacetransformation based on Eq. (26). It can be seen that relative errors are less than 0.1%.

nodes per time-decade), a numerical evaluation of Eq. (25) at 80000 logarithmically spaced values of s ranging from $s_{min} = 10^{-10}\,\text{s}^{-1}$ to $s_{max} = 10^{10}\,\text{s}^{-1}$ gives the results depicted in Fig. 6 (A). It can be seen that the deviation between the analytical solution for the Laplace transformed version of the normalized flux and its numerically constructed analogue is less than 0.1% at each and every instance of s. Using the numerically computed result of $\bar{f}(s)$, performing the Laplace-domain processing on the base of Eq. (23) and a numerical inverse Laplace transformation based on Eqs. (26) and (27) gives an approximation of the desired function $M(t)$ at previously defined instances of the time t. For the result in Fig. 6 (B), 48000 time-instances, evenly distributed on a logarithmic grid from $t_{min} = 10^{-6}\,\text{s}$ to $t_{max} = 10^6\,\text{s}$, have been chosen. For an ideally planar electrode, we achieved a deviation of less than 0.1% between the numerically reconstructed and the analytical version of the function $M(t)$ which corroborates the computational procedure.

4.2. DSDC-algorithm for different surface profiles

Subsequently to the validation of the DSDC-algorithm on a planar electrode, different artifacts of electrode roughness have been introduced into the simulations. These include pyramidal elevations of different height and two hole-structures of different depth and width.

Results for the normalized flux of the pyramidal artifacts are depicted in Fig. 7. It can be seen that a gradually increasing height (and slope) of the pyramidal surface-artifacts, depicted in panels (A) to (C) of Fig. 7, introduces stronger changes in the flux-profile. Moreover, it can be seen that the low-time limit of the normalized flux coincides with the result for planar semi-infinite diffusion in any scenario. This is expected in the context of Eq. (31). However, in contrast to that stands the high-time cutoff (dash-dotted line(s) in Fig. 7). This quantity is shifted towards larger times if the height of the pyramidal surface structures (and thus the degree of roughness) increases. We explain this behavior by the increase in time which is required until the expanding diffusion-zone has compensated the surface profile and mass-transfer can be described as planar semi-infinite. Regarding the double-logarithmic derivatives (gray curves in Fig. 7), one can identify two peaks. One peak, P1, around $10^{-5}\,\text{s}$ and another peak, P2, around $10^{-3}\,\text{s}$. We associate P1 with the diffusive compensation of the individual *stairs* of the pyramidal profile and P2 with the diffusive compensation of the entire pyramidal elevation. This assignment is supported by the fact that P2 is least pronounced in scenario (A), where the pyramidal elevation has the lowest magnitude of all three cases.

Additionally to pyramidal surface structures, two types of hole-structures with different width (200 nm and 400 nm) and depth
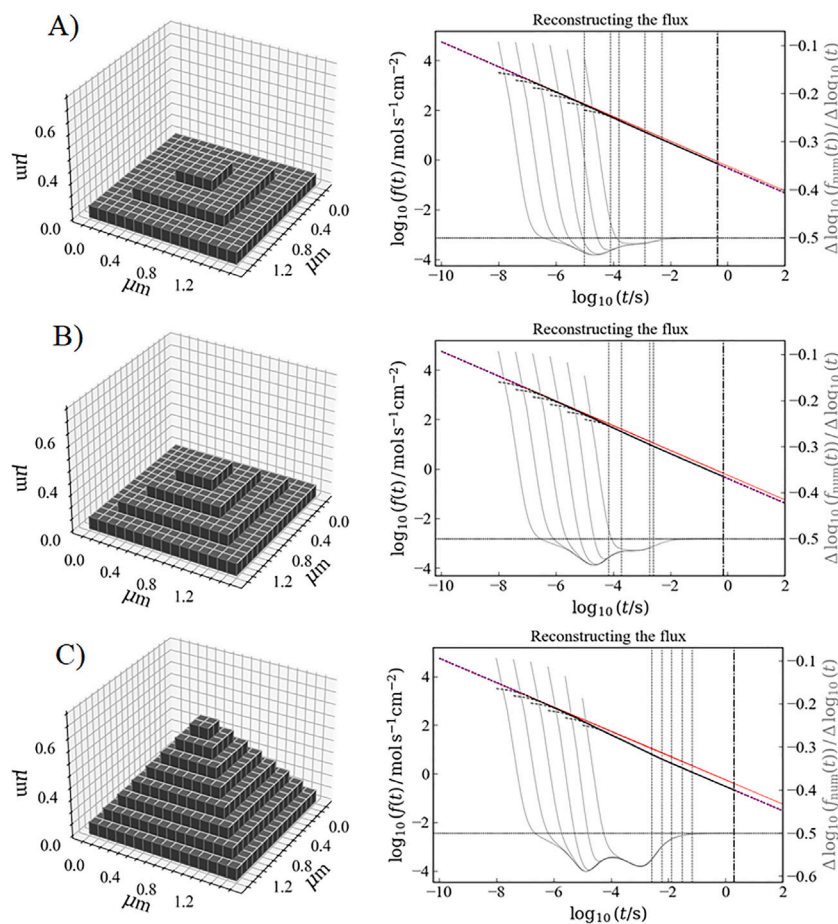
Fig. 7. Illustration of the DS-step for three different pyramidal surface features with different height of (A) 200 nm, (B) 300 nm, and (C) 700 nm. Vertical lines illustrate the cutoff-times which are defined in analogy to Fig. 5. It can be seen that the double-logarithmic derivative of the flux contains two peaks. These are introduced by two different modi of diffusion: (I) diffusion towards the individual edges of the steps of the pyramids and (II) diffusion towards the pyramidal structure before convergence to the planar semi-infinite limit.

(100 nm, 300 nm, 500 nm, 700 nm) have been investigated. These are depicted in Figs. 8 (for width 200 nm) and 9 (for width 400 nm).

It can be seen that the double-logarithmic derivatives of the normalized flux profiles of all recessed hole structures exhibit only one peak (instead of two for the pyramids). Moreover, a comparison of Figs. 8 and 9 reveals that this signal gets shifted towards larger times, if the width of the hole structure increases. Finally, when comparing the hole structures with the pyramidal structures, it can be seen that the simulations converge to the planar semi-infinite limit much earlier (cf. dash-dotted vertices). These three findings can be explained as follows:

The hole structures contain only one type of step site (at the bottom) and, unlike the pyramids, no elevation. Consequently, only one transition in the diffusion profile is expected, which is associated with an *emptying* of the recessed artifacts and which will lead to only one peak in the double-logarithmic derivative of the normalized flux. Since a recessed surface structure with a larger width will contain more active species and can contribute to diffusive mass transfer for longer times, the point in time at which the normalized flux depletes most strongly (*i.e.* the maximum in the derivative) gets shifted to larger time-scales. Finally, once the hole structures are essentially *empty*, mass transfer will be dominated by planar semi-infinite diffusion. This transition from rough-to-planar is, however, inherently different from the scenario of pyramidal structures. There, the diffusion-zone has to expand further into the electrolyte for compensating the elevated artifacts of electrode roughness. This eventually takes more time.

4.3. Reconstructing the mass-transfer functions

Subsequently to the DS-step, the mass-transfer-functions have been reconstructed. This procedure was performed analogue to the planar semi-infinite case outlined in Section 4.1. Firstly, the normalized fluxes have been defined on a logarithmic time-grid spanning from 10^{-20} s to 10^{20} s. The transition regions (between 10^{-7} s to 10^{1} s) for the individual surface profiles (holes and pyramids) are depicted in panels (A), (C) and (E) of Fig. 10. The corresponding mass-transfer functions are depicted in panels (B), (D), and (F) of Fig. 10.

In panels (A), (C), and (E) of Fig. 10, it can be seen that an increasing degree surface roughness, *i.e.* a higher elevation of the pyramids or an increasing depth of the hole structures, will lead to a more pronounced deviation of the normalized flux from the planar semi-infinite case (red curve as reference). Additionally, a later transition to the planar semi-infinite limit is found if the electrode is rougher. Inspecting the mass-transfer functions — particularly for the surfaces containing recessed hole-structures — one can already see that there is a strong correlation between the depth of the surface profile and the values of $M(t)$. More precisely, one may surmise that this particular relation is predominantly linear. For the pyramidal surface structures, no such correlation is found on a first glance.

4.4. Convolutive modeling of CV and quantification of surface roughness

The mass-transfer functions of the individual surface profiles, depicted in Fig. 10, are finally used for the simulation of cyclic voltammetry according to Eq. (28). For reasons of comparability all of the
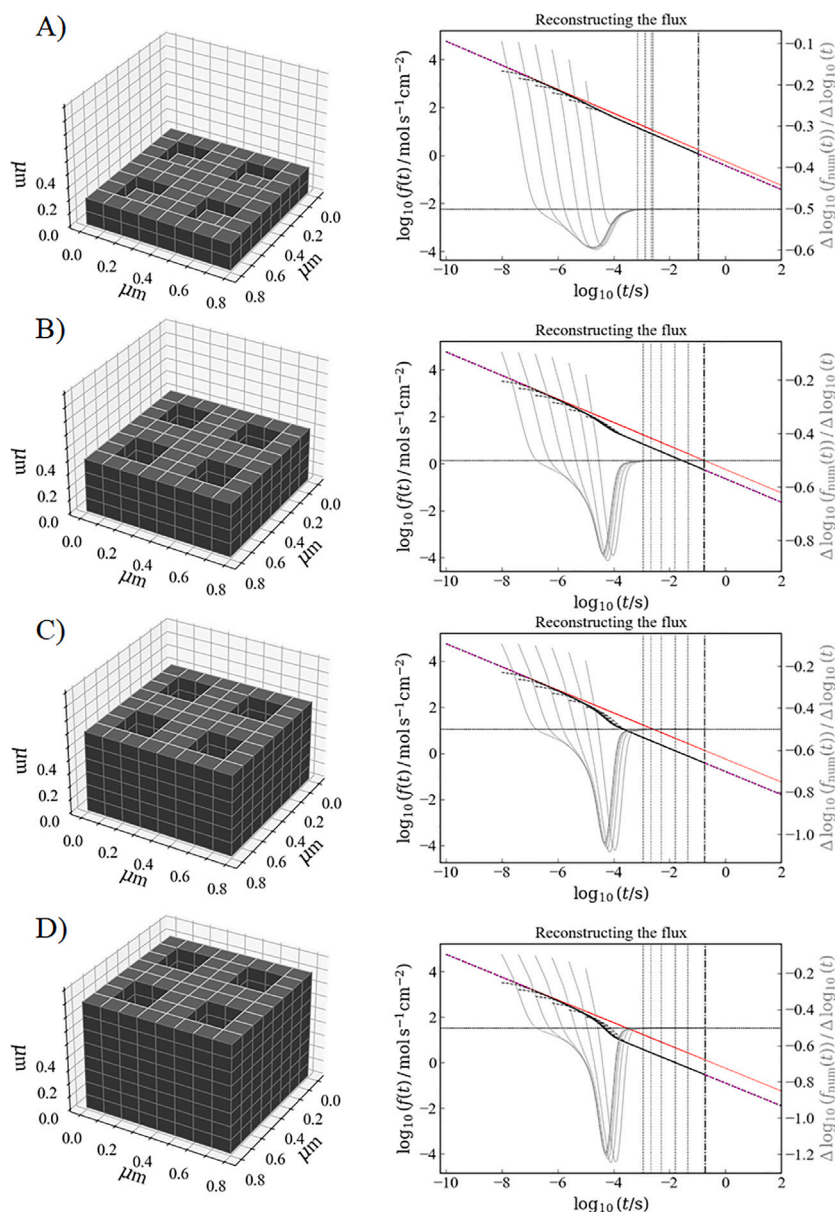
Fig. 8. Illustration of the DS-step for a surface containing hole-structures of a width of 200 nm and depth of (A) 100 nm, (B) 300 nm, and (C) 500 nm, and (D) 700 nm. Vertical lines illustrate the cutoff-times which are defined in analogy to Fig. 5.

following voltammograms will display the dimension-less potentiodynamic flux instead of the current. This quantity was introduced by Matsuda and Ayabe [16] and is given by

$$\chi(t) = \frac{I(t)\sqrt{RT}}{nFA_{\text{geo}}c_{\text{red,bulk}}\sqrt{DnFv}}. \tag{41}$$

It is beneficial to be used here as it normalizes the current to the dynamics of the experiment which are introduced by the potential sweep rate v.

Generally, it is well known that the dynamics of a voltammetric experiment have a strong influence on the electrochemical reversibility of a reaction [8,16]. To overcome the intricate entanglement of electrode kinetics and potentiodynamics, Matsuda and Ayabe [16] have introduced the dimensionless reversibility parameter Λ. Assuming[2] that

oxidized and reduced species have the same diffusion coefficient and unit activity, a simplified version of this quantity is given by

$$\Lambda = k^0\sqrt{\frac{RT}{DnFv}}, \tag{42}$$

where k^0 is the standard heterogeneous rate constant of the electrochemical reaction under investigation.

For the following simulations, we employed two fixed values of the dimensionless reversibility parameter, namely $\Lambda = 15$ for a strictly reversible reaction and $\Lambda = 0.01$ for a quasi-reversible reaction.[3] Eq. (42) was then used for estimating k^0 at a given potential sweep-rate which allows to investigate voltammetric profiles at different timescales without changing the degree of reversibility. The electron transfer coefficient, required for the simulation of CV-curves with Eq. (28), was fixed to $\alpha = 0.5$. Two significantly different potential sweep-rates have been employed, $v = 10$ mV/s and $v = 100$ V/s. Despite the

[2] Otherwise, the original expression for Λ needs to be used which is slightly more complex.

[3] Criteria for reversibility in terms of Λ are outlined in Ref. [16].
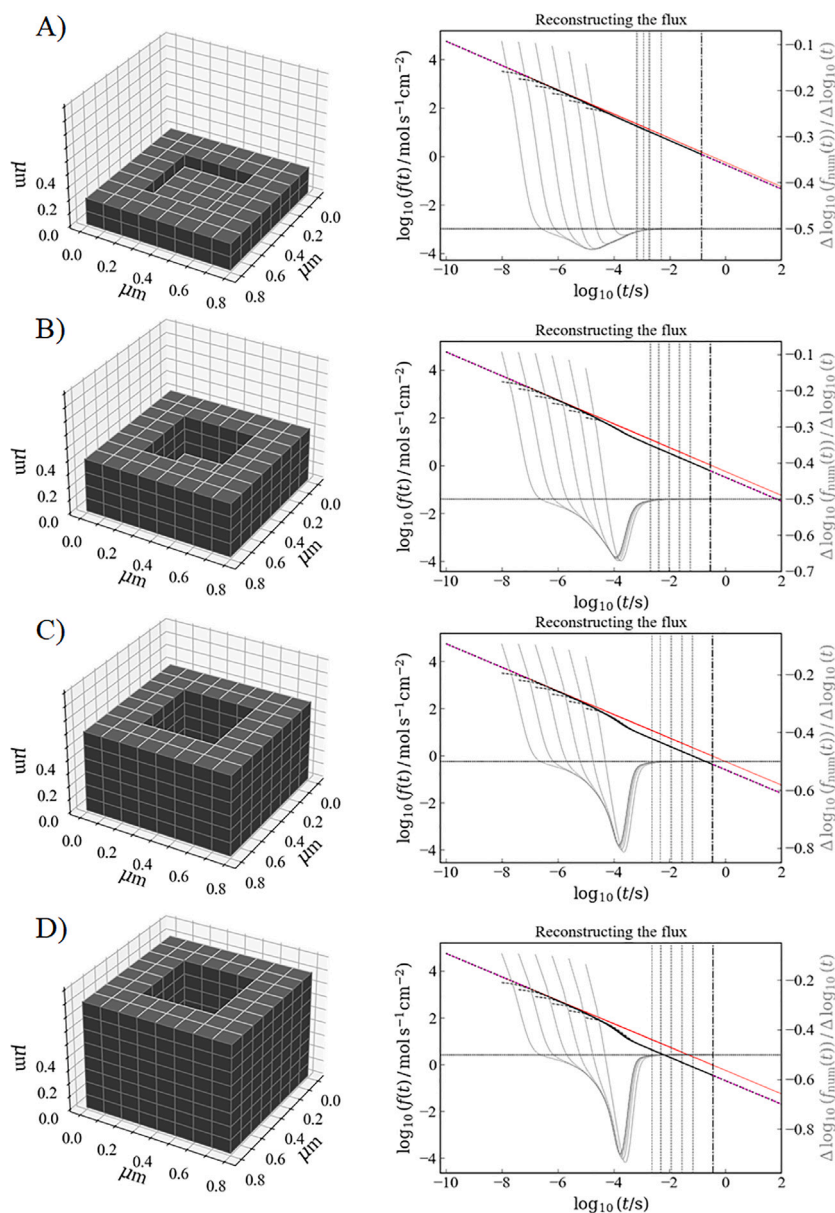
Fig. 9. Illustration of the DS-step for a surface containing hole-structures of a width of 400 nm and depth of (A) 100 nm, (B) 300 nm, and (C) 500 nm, and (D) 700 nm. Vertical lines illustrate the cutoff-times which are defined in analogy to Fig. 5.

fact that sweep-rates as high as $\nu = 100$ V/s are not practical for most voltammetric experiments,[4] they are required here to illustrate the effects of electrode roughness at different timescales as we will show later. Voltammetric responses are depicted in Figs. 11 ($\nu = 10$ mV/s).

Voltammograms depicted in Fig. 11, correspond to the previously introduced pyramidal elevations of different height in panels (A)+(D), recessed hole structures of 200 nm width and different depth in panels (B)+(E) and recessed hole structures of 400 nm width and different depth in panels (C)+(F). Electrochemically quasi-reversible conditions, *i.e.* $\Lambda = 0.01$ was used for the simulations behind panels (A), (B), (C) whereas reversible conditions ($\Lambda = 15$) have been used in the simulations for panels (D), (E), (F). It can be seen that the voltammetric response of an electrochemically reversible reaction is independent of the electrode roughness and all voltammograms coincide. However, for

quasi-reversible reactions, it can be seen that an increasing degree of roughness will lead to a more narrow peak-to-peak separation, usually associated with an increase in the electrode kinetics. This appears intuitive from the perspective that a rough interface will provide more active area for driving the reaction and is in agreement with Ref. [37] where CVs of rough electrodes were computed via digital simulation.

Consequently, one will obtain a putative increase in the heterogeneous rate (constants) which is not seen for a reversible reaction as there is already no kinetic limitation by definition. To confirm this hypothesis, we performed the same simulations as in Fig. 11 (A), (B), (C) with $\Lambda/\psi = 0.01$ instead of $\Lambda = 0.01$, where $\psi = A_{\mathrm{rough}}/A_{\mathrm{geo}}$. Respective results are depicted in Fig. 12. It can be seen that all voltammograms coincide. This leads us to the conclusion that a normalization of Λ by the area-ratio compensates the effect of *additional surface area* and that electrode roughness — at least in this particular example — scales linearly with the kinetics.

To obtain a quantitative explanation for this behavior in terms of convolutive modeling, Eq. (28) needs to be modified. First, one
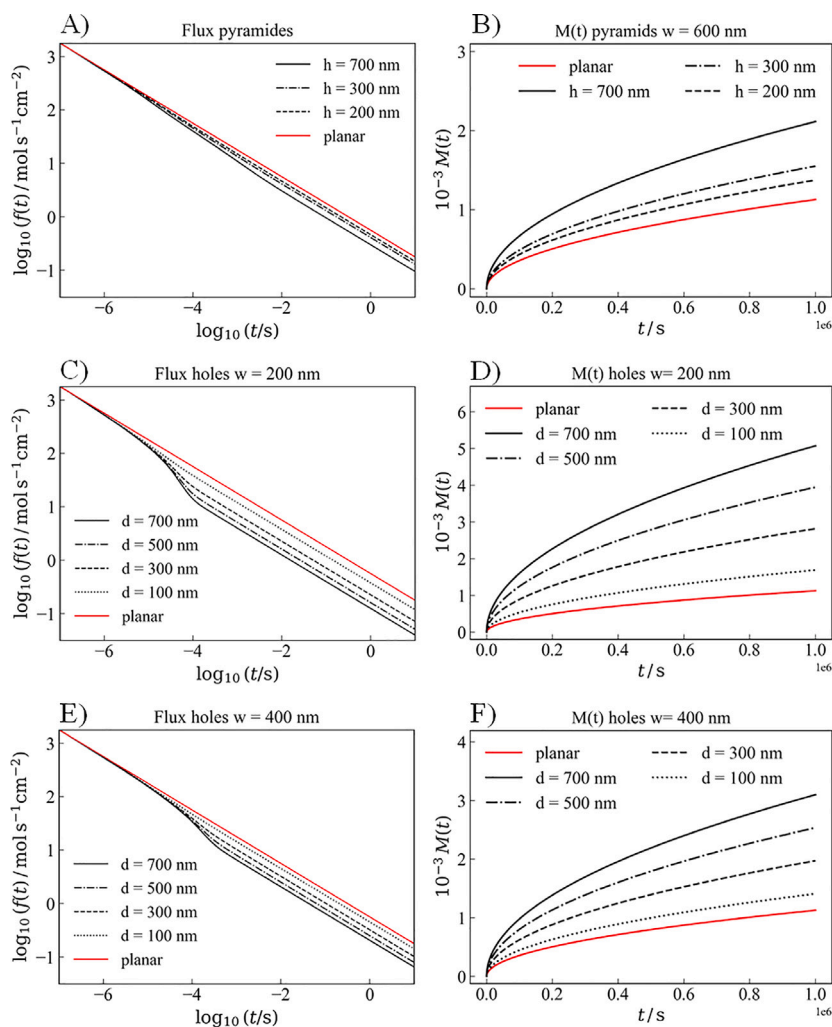
---

[4] Potential sweep-rates of several volts per second will typically result in a strong capacitive contribution which is convoluted with the Faradaic current, distorts the voltammetric profile, and renders a proper analysis very difficult.

Fig. 10. (A), (C), (E) normalized flux responses and (B), (D), (F) corresponding mass-transfer functions for pyramidal elevations and hole-structures with a width of 200 nm and 400 nm, respectively. It can be seen that for the normalized flux a higher elevation of the pyramids or an increasing depth of the hole structures leads to a more pronounced deviation from and a later transition to the planar semi-infinite limit.
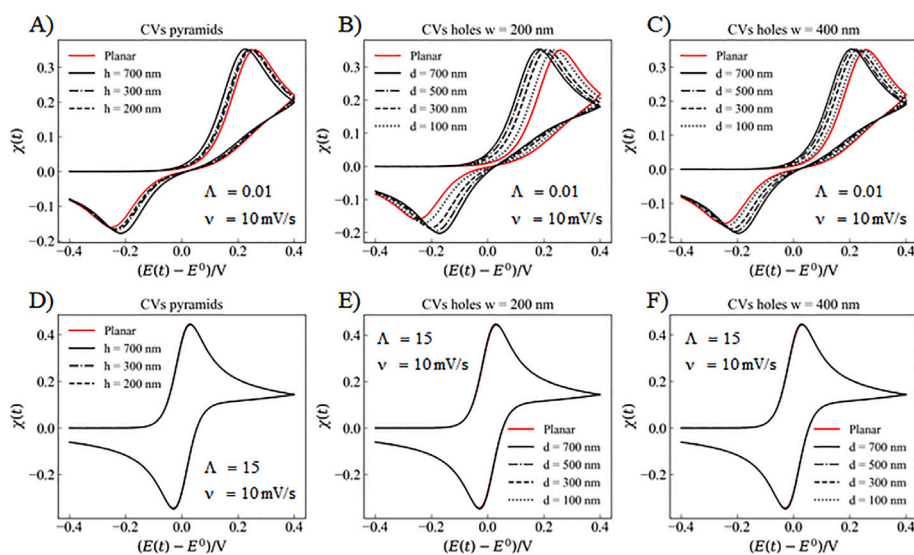

Fig. 11. Voltammograms simulated at a potential sweep-rate of $v = 10\,\text{mV/s}$ for rough electrodes. Roughness is characterized by (A)+(D) pyramidal elevations of different height, recessed hole structures of 200 nm width and different depth, (B)+(E) recessed hole structures of 400 nm width and different depth, and (C)+(F) (cf. Figs. 7–9). Electrochemically quasi-reversible conditions were imposed by setting $\Lambda = 0.01$ and $\alpha = 0.5$ in the simulations via Eq. (28) behind panels (A), (B), (C). In contrast, reversible conditions with $\Lambda = 15$ and independent of α have been used in the simulations for panels (D), (E), (F).
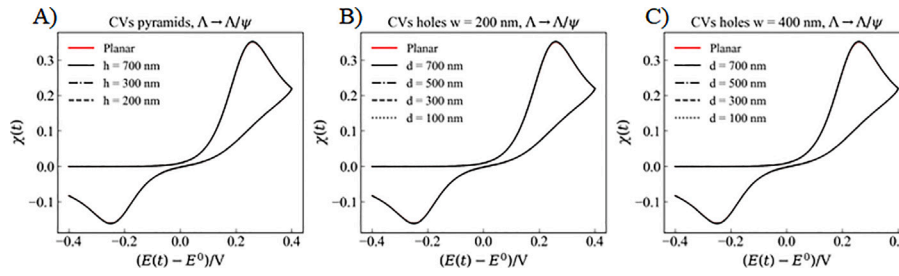
Fig. 12. Voltammograms simulated at a potential sweep-rate of $v = 10\,\text{mV/s}$ for the same structures as in Fig. 11. Electrochemically quasi-reversible conditions which have been imposed by setting $\Lambda = 0.01$ in Fig. 11 have been modified to $\Lambda/\psi = 0.01$, where $\psi = A_{\text{rough}}/A_{\text{geo}}$, the area ratio.
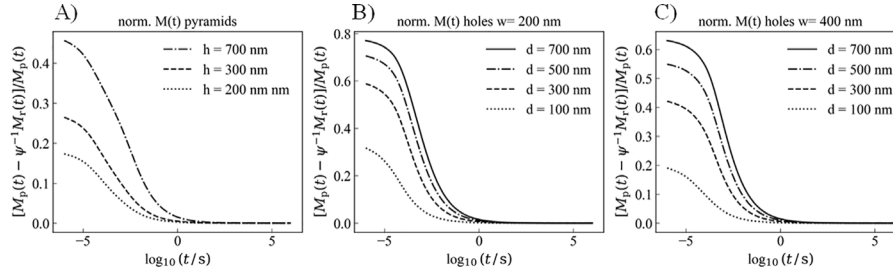

Fig. 13. Relative deviation of the normalized mass-transfer functions $M(t)/\psi$ for (A) pyramidal surface structure, (B) hole structures of 200 nm width and (C) hole structures of 400 nm width at different height and depth.

may substitute the current by the dimension-less potentiodynamic flux which was defined in Eq. (41). This gives

$$\chi(m\Delta t) \approx \frac{\psi - \sqrt{\dfrac{nFv}{RT}}\left[1 + e^{-\xi(m\Delta t)}\right] \cdot S_{\chi,M}}{\dfrac{e^{-\alpha\xi(m\Delta t)}}{\Lambda} + \sqrt{\dfrac{nFv}{RT}}\,M(\Delta t)\left[1 + e^{-\xi(m\Delta t)}\right]}, \qquad (43)$$

leaving the area ratio $\psi = A_{\text{rough}}/A_{\text{geo}}$ in the numerator and introducing Λ into the denominator and using the following recursion sum in terms of χ

$$S_{\chi,M} = \sum_{j=1}^{m-1} \chi(j\Delta t)\left[M((m-j+1)\Delta t) - M((m-j)\Delta t)\right]. \qquad (44)$$

Multiplying numerator and denominator of Eq. (43) by $1/\psi$ will give

$$\chi(m\Delta t) \approx \frac{1 - \sqrt{\dfrac{nFv}{RT}}\left[1 + e^{-\xi(m\Delta t)}\right] \cdot \dfrac{S_{\chi,M}}{\psi}}{\dfrac{e^{-\alpha\xi(m\Delta t)}}{\Lambda\psi} + \sqrt{\dfrac{nFv}{RT}}\,\dfrac{M(\Delta t)}{\psi}\left[1 + e^{-\xi(m\Delta t)}\right]}, \qquad (45)$$

where the term highlighted in red is the sought after scaling relation between electrode kinetics (invoked into Λ) and electrode roughness (characterized by ψ). The terms highlighted in blue are essentially a normalization of the mass-transfer functions by ψ which was investigated further in the context of Fig. 13.

Imposing this particular normalization to the mass-transfer functions and depicting them similar to Fig. 10 will visually lead to a superposition. An alternative — yet more sophisticated representation — is to choose a logarithmic abscissa for the time and to plot the relative deviation of the normalized mass-transfer functions with respect to the analytical solution of the mass-transfer function for planar semi-infinite diffusion. This is displayed in Fig. 13. It can be seen that the relative deviation will almost vanish in all three examples (not to be generalized here) at times greater than 10 s. Considering that all voltammograms in context of Fig. 11 have been computed for a sweep rate of $v = 10\,\text{mV/s}$ on a full potential range of 1.6 V, the time-scale of the experiment reaches at least 160 s. Therefore, all normalized mass-transfer functions have converged to the planar semi-infinite limit (cf. Fig. 13) by that time. This is identified to be the reason why all

reversible CV traces in Fig. 11 and all *kinetically corrected* CV traces in Fig. 12 merge with the planar semi-infinite reference and no additional artifacts of electrode roughness (*e.g.* distortions of the CV-curves similar to porosity-effects) are seen. It is expected that distorting-effects can be observed only if the transition region of the mass-transfer functions coincides with the time-scale of the experiment.

Reducing the time of the (virtual) experiment was essentially achieved by setting the potential sweep-rate to the exceedingly high, and experimentally rather irrelevant, value of 100 V/s in the simulations. Again considering 1.6 V on full scale, this will correspond to a maximum time of 0.016 s — where the transition of the mass-transfer functions to the planar semi-infinite limit is not complete (cf. Fig. 13). Results of the simulations are depicted in terms of dimensionless potentiodynamic flux in Fig. 14. In analogy to Fig. 11 it can be seen that an increasing degree of roughness (*i.e.* deeper holes or higher elevated pyramids) leads to a more narrow peak-to-peak separation for the quasi-reversible scenario of $\Lambda = 0.01$ of panels (A), (B), and (C) in Fig. 14. Additionally, an increase in the peak maximum and a steeper decaying *diffusion tail* are observed in the CVs. In contrast to Fig. 11, these features are also present for the reversible CVs at $\Lambda = 15$ in panels (D), (E), and (F) of Fig. 14. Additionally, the peak-to-peak separation for the reversible CVs becomes less than the thermodynamic limit of 58 mV for semi-infinite diffusion, which appears somewhat odd on a first glance. However, this feature can be explained by considering a *finite diffusion domain effect* which will act as follows. At very low time-scales of the simulation, the relief of the surface profiles is filled with electrolyte. This additional amount of active species is then progressively consumed which gives some *extra current* being added to the planar semi-infinite response. Naturally, this leads to a larger peak magnitude in the CVs. Depending on the electrolyte volume encapsulated in or contributed by the surface roughness, the contribution of this extra current vanishes at a certain point in time. This causes the voltammetric redox-peaks in the CV to deplete faster and is in perfect agreement with the results obtained for a finite diffusion space [9,10,21]. For this reason, it can be concluded that there will be a gradual transition from electrode roughness towards electrode porosity. Since this transition will, however, depend on a multitude of parameters such as the rough surface profile, the diffusion coefficients and the time-scale of the potentiodynamic experiment, an in-depth
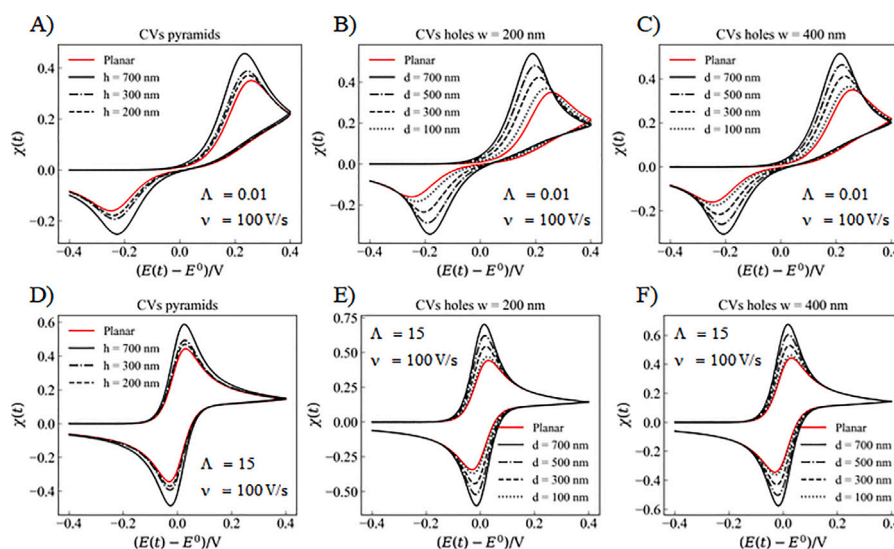
Fig. 14. Voltammograms simulated at a potential sweep-rate of $v = 100$ V/s for rough electrodes. Roughness is characterized by (A)+(D) pyramidal elevations of different height, (B)+(E) recessed hole structures of 200 nm width and different depth, and (C)+(F) recessed hole structures of 400 nm width and different depth (cf. Figs. 7–9). Electrochemically quasi-reversible conditions were imposed by setting $\Lambda = 0.01$ and $\alpha = 0.5$ in the simulations via Eq. (28) behind panels (A), (B), (C). In contrast, reversible conditions with $\Lambda = 15$ and independent of α have been used in the simulations for panels (D), (E), (F).

analysis of this multiparameter-function was not performed yet. However, studying the transition from roughness to porosity will need more careful investigations in future work which can be performed readily with the herein presented DSDC-algorithm.

5. Summary and conclusions

In this paper we have introduced a modified version of the digital-simulation–deconvolution–convolution (DSDC) algorithm to simulate cyclic voltammetry at rough electrode surfaces. The most significant changes to the previous DSDC-algorithm are (I) an adaptive numerical resolution for reducing the computational demand (II) the inclusion of an arbitrarily incremented spatial grid perpendicular to the electrode surface and (III) an optimization of the computationally demanding deconvolution step involving a numerical inverse Laplace transformation based on the Gaver–Stehfest inversion formula. It is demonstrated that the relative deviation between the numerically reconstructed mass-transfer function of a perfectly planar electrode surface and its analytical solution can be kept at less than 0.1% which essentially validated the numerical procedure.

Based on the modified DSDC-algorithm, the effects of electrode roughness have been thoroughly investigated. For this purpose, three different types of surface roughness were considered, namely pyramidal elevations with different height as well as two hole structures with different depth and width.

For common experimental timescales in the range of a few 100 s it is found that for an ideally reversible reaction the effects of electrode roughness on the CV response are insignificant. However, in case of a quasi-reversible (or irreversible) electrochemical reaction, the apparent rate constants are allegedly upscaled by the area ratio $\psi = A_{\text{rough}}/A_{\text{planar}}$. This translates into a lower peak-to-peak separation without a distortion of the voltammetric curves and has a significant consequence for the interpretation of experimental CV data. Since most reactions are not purely reversible, but rather quasi-reversible or even irreversible at the timescale of the experiments, it has to be expected that electrode roughness has a significant impact on the experimental result of voltammetric analyses. Therefore, the experimentalist has to ensure that either (I) the electrode surface under investigation is perfectly planar or (II) the roughness of the electrode is known and kept constant.

For short experimental timescales it is found that the effects of electrode roughness will become similar to effects known from electrode porosity — i.e. a significant distortion of the voltammetric profile will occur. This is associated with an *emptying* of the pore space of the rough surface and becomes gradually insignificant as the experiment progresses.

Both of these two key-findings have been finally explained in terms of convolution sums and mass-transfer functions and were implemented into the semianalytical framework of convolutive modeling. In future work, an in-depth investigation of the gradual transition from electrode roughness to electrode porosity needs to be performed. For this purpose we provide the scripts behind the simulations of this paper as supplementary data as they can be readily used as starting point for such kind of simulations.

CRediT authorship contribution statement

Tim Tichter: Writing – original draft, Visualization, Validation, Supervision, Software, Data curation, Conceptualization. **Alex Tichter:** Writing – original draft, Visualization, Validation, Software. **Dirk Andrae:** Writing – original draft, Formal analysis. **Christina Roth:** Writing – original draft, Supervision, Formal analysis, Conceptualization.

Declaration of competing interest

The authors declare that they have no known competing financial interests or personal relationships that could have appeared to influence the work reported in this paper.

Data availability

The code is available under https://github.com/Polarographica/DSDC_algorithm_rough_electrodes. Other data will be available on request.

Acknowledgments

Appendix A

A.1. Introducing an arbitrarily expanding space-grid

Defining $\Delta z_k = z_{k+1} - z_k$ on an arbitrarily spaced z-grid, a Taylor series expansion of the spatially dependent concentration profile at a spatial node on position i, j, k along the z-direction gives

$$c_{i,j,k+1,t} = c_{i,j,k,t} + \frac{\partial c(x,y,z,t)}{\partial z}\bigg|_{z=z_k} \Delta z_k + \frac{1}{2!}\frac{\partial^2 c(x,y,z,t)}{\partial z^2}\bigg|_{z=z_k} \Delta z_k^2 + \mathcal{O}^3 \quad (46)$$

$$c_{i,j,k-1,t} = c_{i,j,k,t} - \frac{\partial c(x,y,z,t)}{\partial z}\bigg|_{z=z_k} \Delta z_{k-1} + \frac{1}{2!}\frac{\partial^2 c(x,y,z,t)}{\partial z^2}\bigg|_{z=z_k} \Delta z_{k-1}^2 - \mathcal{O}^3. \quad (47)$$

The alternating sign in Eq. (47) results from the definition of Δz_{k-1} as positive quantity and the reverse-stepping in space. This results in a positive sign for all even terms. Particularly note that Δz_{k-1} is not necessarily equal to Δz_k since the grid is arbitrarily spaced. Omitting cubic (and higher order) terms, Eqs. (46) and (47) can be rearranged and into a 2×2 matrix–vector product according to

$$\underline{\underline{Z}}\,\underline{\delta} = \underline{\Delta}, \quad (48)$$

where

$$\underline{\underline{Z}} = \begin{pmatrix} -\Delta z_{k-1} & 0.5\Delta z_{k-1}^2 \\ \Delta z_k & 0.5\Delta z_k^2 \end{pmatrix} \quad (49)$$

$$\underline{\delta} = \begin{pmatrix} \dfrac{\partial c(x,y,z,t)}{\partial z}\bigg|_{z=z_k} \\[2mm] \dfrac{\partial^2 c(x,y,z,t)}{\partial z^2}\bigg|_{z=z_k} \\[2mm] . \end{pmatrix} \quad (50)$$

$$\underline{\Delta} = \begin{pmatrix} c_{i,j,k-1,t} - c_{i,j,k,t} \\ c_{i,j,k+1,t} - c_{i,j,k,t} \end{pmatrix} \quad (51)$$

Finding the approximation of the spatial derivatives along the z-direction at the nodes z_k is then performed by computing the inverse of the matrix $\underline{\underline{Z}}$.

Subsequently, the individual coefficients for a first or second derivative can be obtained by performing the following dot product

$$\underline{\delta} = \underline{\underline{Z}}^{-1}\,\underline{\Delta}. \quad (52)$$

Since the right hand side of Eq. (1) requires approximations for second spatial derivatives, only the second line of the matrix $\underline{\underline{Z}}^{-1}$ is required and referred to as $\underline{\underline{Z}}^{-1}[1, : :]$.[5] This gives

$$\frac{\partial^2 c(x,y,z,t)}{\partial z^2}\bigg|_{z=z_k} \approx \underline{\underline{Z}}^{-1}[1,0](c_{i,j,k-1,t} - c_{i,j,k,t}) + \underline{\underline{Z}}^{-1}[1,1](c_{i,j,k+1,t} - c_{i,j,k,t})$$
$$= \alpha_k c_{i,j,k-1,t} + \beta_k\, c_{i,j,k,t} + \gamma_k\, c_{i,j,k+1,t},$$
$$(53)$$

where the coefficients in Eq. (53) are defined by $\alpha_k = \underline{\underline{Z}}^{-1}[1,0]$ and $\beta_k = -(\underline{\underline{Z}}^{-1}[1,0] + \underline{\underline{Z}}^{-1}[1,1])$ and $\gamma_k = \underline{\underline{Z}}[1,1]$. It has to be underlined that these coefficients are computed on the points adjacent to z_k. For an arbitrarily spaced grid, however, these values need to be explicitly computed for each and every node — *i.e.* also for the points centered at $k-1$, $k+1$ and so on.

Appendix B. Supplementary data

Supplementary material related to this article can be found online at https://doi.org/10.1016/j.electacta.2024.145175.

---

[5] This notation is used to preserve nomenclature of the Python programming language which is used for the simulations. The first entry in the square brackets refers to lines, the second to columns, such that, *e.g.* $\underline{\underline{Z}}^{-1}[0,1]$ means the zeroth line and the first column.

References

[1] B. Li, M. Gu, Z. Nie, Y. Shao, Q. Luo, X. Wei, X. Li, J. Xiao, C. Wang, V. Sprenkle, W. Wang, Bismuth nanoparticle decorating graphite felt as a high-performance electrode for an all-vanadium redox flow battery, Nano Lett. 13 (2013) 1330–1335, http://dx.doi.org/10.1021/nl400223v.

[2] D.J. Suárez, Z. Gonzalez, C. Blanco, M. Granda, R. Menendez, S. Ricardo, Graphite Felt Modified with Bismuth Nanoparticles as Negative Electrode in a Vanadium Redox Flow Battery, ChemSusChem 7 (2014) 914–918, http://dx.doi.org/10.1002/cssc.201301045.

[3] X. Yang, T. Liu, C. Xu, H. Zhang, X. Li, H. Zhang, The catalytic effect of bismuth for VO^{2+}/VO_2^{+} and V^{3+}/V^{2+} redox couples in vanadium flow batteries, J. Energy Chem. 26 (2017) 1–7, http://dx.doi.org/10.1016/j.jechem.2016.09.007.

[4] M. Gebhard, T. Tichter, J. Schneider, J. Mayer, A. Hilger, M. Osenberg, M. Rahn, I. Manke, C. Roth, On the stability of bismuth in modified carbon felt electrodes for vanadium redox flow batteries: An in-operando X-ray computed tomography study, J. Power Sources 478 (2020) 232861, http://dx.doi.org/10.1016/j.jpowsour.2020.228695.

[5] M. Schnucklake, M. Cheng, M. Maleki, C. Roth, A mini-review on decorating, templating of commercial and electrospinning of new porous carbon electrodes for vanadium redox flow batteries, J. Phys. Mater. 4 (2021) 032007, http://dx.doi.org/10.1088/2515-7639/abf1a9.

[6] Y. Wen, T.P. Neville, A. Jorge Sobrido, P.R. Shearing, D.J. Brett, R. Jervis, Bismuth concentration influenced competition between electrochemical reactions in the all-vanadium redox flow battery, J. Power Sources 566 (2023) 232861, http://dx.doi.org/10.1016/j.jpowsour.2023.232861.

[7] M. Cheng, T. Kottakkat, C. Roth, Dynamic hydrogen bubble template electrodeposited bi on graphite felt and the effect of its post-processing in vanadium redox flow batteries, J. Mater. Chem. A 11 (2023) 13341–13352, http://dx.doi.org/10.1039/D2TA09839C.

[8] R.S. Nicholson, Theory and application of cyclic voltammetry for measurement of electrode reaction kinetics, Anal. Chem. 37 (1965) 1351–1355, http://dx.doi.org/10.1021/ac60230a016.

[9] K. Aoki, K. Tokuda, H. Matsuda, Theory of linear sweep voltammetry with finite diffusion space, J. Electroanal. Chem. Interfacial Electrochem. 146 (1983) 417–424, http://dx.doi.org/10.1016/S0022-0728(83)80601-9.

[10] K. Aoki, K. Tokuda, H. Matsuda, Theory of linear sweep voltammetry with finite diffusion space: Part II. Totally irreversible and quasi-reversible cases, J. Electroanal. Chem. Interfacial Electrochem. 160 (1984) 33–45, http://dx.doi.org/10.1016/S0022-0728(84)80113-8.

[11] L.K. Bieniasz, Automatic solution of integral equations describing electrochemical transients under conditions of internal cylindrical diffusion, J. Electroanal. Chem. 700 (2013) 30–39, http://dx.doi.org/10.1016/j.jelechem.2013.04.010.

[12] L.K. Bieniasz, Automatic solution of integral equations describing electrochemical transients under conditions of internal spherical diffusion, J. Electroanal. Chem. 694 (2013) 104–113, http://dx.doi.org/10.1016/j.jelechem.2013.01.043.

[13] K.B. Oldham, Convolution: a general electrochemical procedure implemented by a universal algorithm, Anal. Chem. 58 (1986) 2296–2300, http://dx.doi.org/10.1021/ac00124a040.

[14] P.J. Mahon, K.B. Oldham, Incorporating electrode kinetics into the convolutive modeling of reactions at planar, cylindrical and spherical electrodes, Electrochim. Acta 46 (2001) 953–965, http://dx.doi.org/10.1016/S0013-4686(00)00680-0.

[15] K.B. Oldham, J.C. Myland, Modelling cyclic voltammetry without digital simulation, Electrochim. Acta 56 (2011) 10612–10625, http://dx.doi.org/10.1016/j.electacta.2011.05.044.

[16] H. Matsuda, Y. Ayabe, Zur theorie der randles-Ševčík'schen kathodenstrahl-polarographie, Z. Elektrochem. 59 (1954) 494–503, http://dx.doi.org/10.1002/bbpc.19550590605.

[17] K. Aoki, K. Honda, K. Tokuda, H. Matsuda, Voltammetry at microcylinder electrodes: Part I. Linear sweep voltammetry, J. Electroanal. Chem. Interfacial Electrochem. 182 (1985) 267–279, http://dx.doi.org/10.1016/0368-1874(85)87005-2.

[18] T. Tichter, D. Andrae, C. Roth, Analytical solutions for the diffusive mass transfer at cylindrical and hollowcylindrical electrodes with reflective and transmissive boundary conditions, J. Electroanal. Chem. 897 (2021) 115565, http://dx.doi.org/10.1016/j.jelechem.2021.115565.

[19] C. Montella, LSV modelling of electrochemical systems through numerical inversion of Laplace transforms. I – the GS–LSV algorithm, J. Electroanal. Chem. 614 (2007) 121–130, http://dx.doi.org/10.1016/j.jelechem.2007.11.010.

[20] C. Montella, J.P. Diard, New approach of electrochemical systems dynamics in the time-domain under small-signal conditions. I. A family of algorithms based on numerical inversion of Laplace transforms, J. Electroanal. Chem. 623 (2008) 29–40, http://dx.doi.org/10.1016/j.jelechem.2007.11.010.

[21] T. Tichter, J. Schneider, D. Andrae, M. Gebhard, C. Roth, Universal algorithm for simulating and evaluating cyclic voltammetry at macroporous electrodes by considering random arrays of microelectrodes, ChemPhysChem 21 (2019) 428–441, http://dx.doi.org/10.1002/cphc.201901113.

[22] T. Tichter, D. Andrae, J. Schneider, M. Gebhard, A. Hilger, I. Manke, C. Roth, Real-space simulation of cyclic voltammetry in carbon felt electrodes by combining micro X-ray CT data, digital simulation and convolutive modeling, Electrochim. Acta 353 (2020) 136487, http://dx.doi.org/10.1002/cphc.201901113.

[23] H. Stehfest, Numerical inversion of Laplace transforms: Algorithm 368, Commun. ACM 13 (1970) 47–49.

[24] D. Britz, J. Strutwolf, Digital Simulation in Electrochemistry, Springer International Publishing, Switzerland, 2016, http://dx.doi.org/10.1007/978-3-319-30292-8.

[25] J. Heinze, M. Störzbach, J. Mortensen, Digital simulation of cyclic voltammetric curves by the implicit crank–nicolson technique, J. Electroanal. Chem. 165 (1983) 61–70, http://dx.doi.org/10.1016/S0022-0728(84)80086-8.

[26] M. Störzbach, J. Heinze, The crank nicolson technique — an efficient algorithm for the simulation of electrode processes at macro- and microelectrodes, J. Electroanal. Chem. 346 (1993) 1–27, http://dx.doi.org/10.1016/0022-0728(93)85001-W.

[27] J. Douglas, Alternating direction methods for three space variables, Numer. Math. 4 (1962) 41–63, http://dx.doi.org/10.1007/BF01386295.

[28] T.-Y. Wang, Y.-M. Lee, C. Chen, 3D thermal-ADI - an efficient chip-level transient thermal simulator, in: Association for Computing Machinery, Proceedings of the 2003 International Symposium on Physical Design, 2003, pp. 10–17, http://dx.doi.org/10.1145/640000.640007.

[29] L.H. Thomas, Elliptic problems in linear differential equations over a network, 1949, Watson Science Computer Laboratory Report.

[30] A. Talbot, The accurate numerical inversion of Laplace transforms, J. Appl. Math. 23 (1979) 97–120, http://dx.doi.org/10.1093/imamat/23.1.97.

[31] J.A.C. Weideman, N.L. Trefethen, Parabolic and hyperbolic contours for computing the bromwich integral, Math. Comp. 76 (2007) 1341–1356, http://dx.doi.org/10.1090/S0025-5718-07-01945-X.

[32] B. Dingfelder, J.A.C. Weideman, An improved talbot method for numerical Laplace transform inversion, Numer. Algorithms 68 (2015) 167–183, http://dx.doi.org/10.1007/s11075-014-9895-z.

[33] C. Montella, Re-examination of the potential-step chronoamperometry method through numerical inversion of Laplace transforms. I. General formulation and numerical solution, J. Electroanal. Chem. 633 (2009) 35–44, http://dx.doi.org/10.1016/j.jelechem.2009.04.019.

[34] R.S. Nicholson, I. Shain, Theory of stationary electrode polarography single scan and cyclic methods applied to reversible, irreversible, and kinetic systems, Anal. Chem. 36 (1964) 706–723, http://dx.doi.org/10.1021/ac60210a007.

[35] C. Montella, LSV/CV modelling of electrochemical reactions with interfacial CPE behaviour, using the generalised Mittag–Leffler function, J. Electroanal. Chem. 667 (2012) 38–47, http://dx.doi.org/10.1016/j.jelechem.2011.12.010.

[36] A.J. Bard, L.R. Faulkner, Electrochemical methods: Fundamentals and applications, Wiley and Sons, 2001, http://dx.doi.org/10.1023/A:1021637209564.

[37] D. Menshykau, I. Streeter, R.G. Compton, Influence of electrode roughness on cyclic voltammetry, J. Phys. Chem. C 112 (2008) 14428–14438, http://dx.doi.org/10.1021/jp8047423.